

THE PHYSICS OF PROTONEUTRON STAR WINDS: IMPLICATIONS FOR *R*-PROCESS NUCLEOSYNTHESIS

TODD A. THOMPSON

Department of Physics, The University of Arizona, Tucson, AZ 85721
thomp@physics.arizona.edu

ADAM BURROWS

Steward Observatory, The University of Arizona, Tucson, AZ 85721
burrows@jupiter.as.arizona.edu

BRADLEY S. MEYER

Department of Physics and Astronomy, Clemson University, Clemson, SC 29634-0978
mbradle@ces.clemson.edu

ACCEPTED TO APJ: July 28, 2001

ABSTRACT

We solve the general-relativistic steady-state eigenvalue problem of neutrino-driven protoneutron star winds, which immediately follow core-collapse supernova explosions. We provide velocity, density, temperature, and composition profiles and explore the systematics and structures generic to such a wind for a variety of protoneutron star characteristics. Furthermore, we derive the entropy, dynamical timescale, and neutron-to-seed ratio in the general relativistic framework essential in assessing this site as a candidate for *r*-process nucleosynthesis. Generally, we find that for a given mass outflow rate (\dot{M}), the dynamical timescale of the wind is significantly shorter than previously thought.

We argue against the existence or viability of a high entropy ($\gtrsim 300$ per k_B per baryon), long dynamical timescale *r*-process epoch. In support of this conclusion, we model the protoneutron star cooling phase, calculate nucleosynthetic yields in our steady-state profiles, and estimate the integrated mass loss. We find that transonic winds enter a high entropy phase only with very low \dot{M} ($\lesssim 1 \times 10^{-9} M_\odot s^{-1}$) and extremely long dynamical timescale ($\tau_p \gtrsim 0.5$ seconds). Our results support the possible existence of an early *r*-process epoch at modest entropy (~ 150) and very short dynamical timescale, consistent in our calculations with a very massive or very compact protoneutron star that contracts rapidly after the preceding supernova. We explore possible modifications to our models, which might yield significant *r*-process nucleosynthesis generically.

Finally, we speculate on the effect of fallback and shocks on both the wind physics and nucleosynthesis. We find that a termination or reverse shock in the wind, but exterior to the wind sonic point, may have important nucleosynthetic consequences. The potential for the *r*-process in protoneutron star winds remains an open question.

Subject headings: Winds, neutrinos, supernovae, neutron stars, nucleosynthesis

1. INTRODUCTION

The successful two-dimensional Type-II supernova simulation of Burrows, Hayes, and Fryxell (1995) shows clearly a post-explosion neutrino-driven wind, emerging approximately half a second after bounce. The convective plumes and fingers due to Rayleigh-Taylor instabilities that accompany shock re-ignition in the gain region are pushed out and cleared from the area closest to the neutron star by the pressure of the neutrino-driven wind. The last 50 milliseconds (ms) of the simulation show that a nearly spherically symmetric wind has established itself as the protoneutron star, newly born, begins its Kelvin-Helmholtz cooling phase.¹ Although these simulations employed only crude neutrino transport, did not address the issue of fallback, and did not study the wind as a function of progenitor mass and structure, they are suggestive of a general phenomenon that might naturally accompany many core-collapse supernovae.

¹ See these 2D simulations at <http://www.astrophysics.arizona.edu/movies.html>.

Some multiple of 10^{53} erg will be lost via neutrino radiation by the protoneutron star as it cools. A small fraction of that energy will be deposited in the surface layers of the nascent neutron star, heating and driving material from its surface. Although the wind is interesting in its own right, hydrodynamically and as a phenomenon that attends both the supernova and the Kelvin-Helmholtz cooling phase, perhaps its most important ramification is the potential production of $\sim 50\%$ of all the nuclides above the iron group in rapid(*r*) neutron-capture nucleosynthesis.

In the *r*-process, rapid interaction of neutrons with heavy, neutron-rich, seed nuclei allows a neutron capture-disintegration equilibrium to establish itself among the isotopes of each element. Beta decays occur on a longer timescale and increase the nuclear charge. For sufficiently large neutron-to-seed ratio, the ‘nuclear flow’ proceeds to the heaviest nuclei, forming abundance peaks at $A \sim 80, 130$, and 195 (Burbidge et al. 1957; Wallerstein et al. 1997). The neutron-to-seed ra-

tio itself is largely set by the dynamical timescale (τ_ρ ; see eq. 32), entropy (s), and neutron richness in the earlier phase of the expansion (Hoffman, Woosley, and Qian 1997; Meyer and Brown 1997; Freiburghaus et al. 1999). While the nuclear physics is fairly well understood, the astrophysical site has not been unambiguously established. Currently, neutron star mergers (Freiburghaus, Rosswog, and Thielemann 1999, and references therein; Rosswog et al. 1999) and protoneutron star winds (Meyer et al. 1992; Woosley and Hoffman 1992; Woosley et al. 1994; Qian and Woosley 1996; Hoffman, Woosley, and Qian 1997; Otsuki et al. 2000) are considered the most viable candidates.

In addition to attaining the requisite neutron-to-seed ratios, dynamical timescales, and temperatures, the astrophysical site must consistently reproduce the observed solar abundance pattern of *r*-process elements with $A \gtrsim 135$. Recent observations of neutron-capture elements in ultra-metal-poor halo stars (Burris et al. 2000; McWilliam et al. 1995a,b; Sneden et al. 1996; Cowan et al. 1996; Westin et al. 2000; Hill et al. 2001) show remarkable agreement with the solar *r*-process abundance pattern in this mass range. This suggests a universal mechanism for producing the second and third abundance peaks, which acts early in the chemical enrichment history of the galaxy. In this paper, beyond addressing the physical nature and systematics of the wind, we investigate its potential as a site for *r*-process nucleosynthesis up to and beyond the third abundance peak.

Duncan, Shapiro, & Wasserman (1986) were the first to address the physics of steady-state neutrino-driven neutron star winds. Although interested in the relative importance of the neutrino and photon luminosity in determining the wind dynamics, they also identified some of the basic systematics and scaling relations generic to the problem. More recent investigations have focused less on the general physics of the wind and more on its potential nucleosynthetic yield. Woosley et al. (1994) conducted the first such detailed study. They followed the nucleosynthesis in a protoneutron star wind that emerged in a one-dimensional post-supernova environment. Approximately 18 seconds after collapse and explosion, their model attained entropies of ~ 400 (throughout, we quote entropy per k_B per baryon), long dynamical timescales, and electron fraction (Y_e) in the range $0.36 - 0.44$. However, in their model the supernova shock reached only 50,000 km at these late times. In turn, this external boundary caused the wind material to move slowly. It remained in the heating regime for an extended period, thus raising the entropy above what any simulation or analytical calculation has since obtained. Although the *r*-process proceeded to the third abundance peak in their calculation, nuclei in the mass range near $A \sim 90$ (particularly, ^{88}Sr , ^{89}Y , and ^{90}Zr) were overproduced by more than a factor of 100.

Takahashi, Witt, & Janka (1994) conducted a similar investigation, but did not attain the entropies of Woosley et al. (1994). In fact, they fell short by a factor of ~ 5 . Later, Qian & Woosley (1996) showed that for reasonable protoneutron star characteristics, including post-Newtonian corrections, an entropy of 400 is unrealistic. Qian & Woosley (1996) also provided many analytical scaling relations that have since framed the discussion of neutrino-driven winds. Following this work, Hoffman, Woosley, & Qian (1997) conducted nucleosynthetic calculations in the wind models of Qian & Woosley (1996). They concluded that the standard wind models of Qian & Woosley (1996) did not produce third peak *r*-process nu-

cleosynthesis. They also employed an adiabatic cooling prescription to survey the parameter space relevant to protoneutron star winds and noted several important systematics in the nucleosynthesis. Particularly, they identified a low entropy (~ 120), fast timescale ($\tau_\rho \sim 2$ ms), and *high* electron fraction ($Y_e \gtrsim 0.48$) window where third peak *r*-process could take place (see their Fig. 10).

Cardall & Fuller (1997) generalized some of the scaling relations presented in Qian & Woosley (1996) to include general relativity and found significant enhancements in the entropy and dynamical timescale of the wind in this framework. Recently, Otsuki et al. (2000) have sought to solve the general-relativistic wind equations and to conduct *r*-process calculations in the winds they obtained. They concluded that *r*-process nucleosynthesis can proceed to the third abundance peak at $A \sim 195$ for a protoneutron star with radius 10 km, a gravitational mass of $2 M_\odot$, and total neutrino luminosity of 10^{52} erg s $^{-1}$. These conditions produce modest entropies ($s \sim 140$) and fast dynamical timescales ($\tau_\rho \sim 2 - 3$ ms). Although a significant parameter in protoneutron star winds, Y_e was fixed by hand in their calculations. Furthermore, they employed a simple equation of state and, in the context of the transonic wind problem, an unphysical external boundary condition.

These uncertainties and ambiguities in the conclusions of previous groups suggest that a re-evaluation is in order. Our goal in this paper is to solve the full eigenvalue problem of the steady-state transonic wind problem in general relativity, employing physical boundary conditions. Using this formalism, we survey the relevant parameter space, identify the major systematic trends, and explore some of the particulars of the general-relativistic treatment. We then use these steady-state solutions to model the whole of the Kelvin-Helmholtz cooling phase, including radial contraction of the protoneutron star, as well as the evolution of the neutrino luminosity and average neutrino energy. We estimate the total amount of material ejected during this cooling epoch, and put significant constraints on the range of entropies and dynamical timescales that might actually occur in Nature. In addition, for a subset of the models generated, we calculate the total nucleosynthetic yield as a function of atomic mass.

In §2, we present the fundamental equations for a time-independent neutrino-driven wind (general-relativistic and Newtonian), including the equation for the evolution of the electron fraction. In addition, we present the integrals of the motion and a discussion of the equation of state we employ. In §3, we describe our solution to the wind problem using an iterative relaxation procedure on an adjustable radial grid and the necessary boundary conditions. In §4, we present the neutrino heating rates used in this study, review the effects of general relativity, discuss potential modifications to the energy deposition rates, and explore (approximately) the effects of transport. In §5, we present our results for the wind problem itself. The wind structures and general characteristics as a function of neutron star mass, radius, and neutrino spectral character are explored. We cover the entire relevant parameter space and include some modifications to the power laws presented in Qian & Woosley (1996). In §6, we use our steady-state wind results to construct a sequence of such models that represent the time evolution of the wind during the protoneutron star cooling phase. We estimate the total mass ejected for a given evolutionary trajectory and put useful constraints on possible epochs of

r-process nucleosynthesis. In §7, we present nucleosynthetic results from a subset of our wind trajectories. In §8, we discuss reasonable modifications to our wind models that might yield a successful *r*-process, including changes to the energy deposition function. Finally, in §9 we review our results, summarizing the constraints our calculations impose on the viability of the protoneutron star wind as the astrophysical site of the *r*-process. Furthermore, we speculate on the effects of progenitor structures and fallback, as well as hydrodynamical and transport considerations left to be addressed in future work.

2. THE STEADY-STATE WIND EQUATIONS

The time-independent hydrodynamical equations for flow in a Schwarzschild spacetime can be written in the form (Nobili, Turolla, and Zampieri 1991; Flammang 1982)

$$\frac{1}{vy} \frac{d(vy)}{dr} + \frac{1}{\rho} \frac{d\rho}{dr} + \frac{2}{r} = 0, \quad (1)$$

$$\frac{1}{y} \frac{dy}{dr} + \frac{1}{\varepsilon + P} \frac{dP}{dr} = 0, \quad (2)$$

and

$$\frac{d\varepsilon}{dr} - \frac{\varepsilon + P}{\rho} \frac{d\rho}{dr} + \rho \frac{\dot{q}}{vy} = 0, \quad (3)$$

where $u_r (= vy)$ is the radial component of the fluid four-velocity, v is the velocity of the matter measured by a stationary observer,

$$y = \left(\frac{1 - 2GM/rc^2}{1 - v^2/c^2} \right)^{1/2}, \quad (4)$$

$\epsilon (= \rho c^2 + \rho \epsilon)$ is the total mass-energy density, ρ is the rest-mass density, P is the pressure, ϵ is the specific internal energy, and \dot{q} is the energy deposition rate per unit mass. These equations assume that the mass of the wind is negligible. Although not readily apparent in the form above, eqs. (1)–(3) exhibit a critical point when v equals the local speed of sound. In order to make the solution to this system tractable and the critical point manifest we recast the equations as

$$\begin{aligned} \frac{\partial v}{\partial r} &= \frac{v}{2r} \left[\frac{v_e^2}{y^2} \left(\frac{1 - c_s^2/c^2}{c_s^2 - v^2} \right) - 4c_s^2 \left(\frac{1 - v^2/c^2}{c_s^2 - v^2} \right) \right] \\ &\quad + \frac{D}{C_V T} \frac{\dot{q}}{y} \left(\frac{1 - v^2/c^2}{c_s^2 - v^2} \right), \end{aligned} \quad (5)$$

$$\frac{\partial \rho}{\partial r} = \frac{2\rho}{r} \left(\frac{v^2 - v_e^2/4y^2}{c_s^2 - v^2} \right) - \frac{\rho}{(vy) C_V T} \frac{D}{c_s^2 - v^2} \frac{\dot{q}}{c_s^2 - v^2}, \quad (6)$$

and

$$\begin{aligned} \frac{\partial T}{\partial r} &= \frac{2}{r\rho} \frac{D}{C_V} \frac{(P + \varepsilon)}{c^2} \left(\frac{v^2 - v_e^2/4y^2}{c_s^2 - v^2} \right) \\ &\quad + \frac{\dot{q}}{C_V (vy)} \left(\frac{(1 - D/c^2)c_T^2 - v^2}{c_s^2 - v^2} \right). \end{aligned} \quad (7)$$

In the above expressions, C_V is the specific heat at constant volume, c_s is the local adiabatic sound speed, c_T is the isothermal sound speed, $v_e = (2GM/r)^{1/2}$, M is the protoneutron star gravitational mass, and

$$D = c^2 \frac{T}{\varepsilon + P} \frac{\partial P}{\partial T} \Big|_{\rho}. \quad (8)$$

Taking the limits $v/c \ll 1$ and $c_s/c \ll 1$ we recover the Newtonian wind equations in critical form;

$$\frac{\partial v}{\partial r} = \frac{v}{2r} \left(\frac{v_e^2 - 4c_s^2}{c_s^2 - v^2} \right) + \frac{D}{C_V T} \frac{\dot{q}}{c_s^2 - v^2}, \quad (9)$$

$$\frac{\partial \rho}{\partial r} = \frac{2\rho}{r} \left(\frac{v^2 - v_e^2/4}{c_s^2 - v^2} \right) - \frac{\rho}{v C_V T} \frac{D}{c_s^2 - v^2} \frac{\dot{q}}{c_s^2 - v^2} \quad (10)$$

and

$$\frac{\partial T}{\partial r} = \frac{2}{r} \frac{D}{C_V} \left(\frac{v^2 - v_e^2/4}{c_s^2 - v^2} \right) + \frac{\dot{q}}{C_V v} \left(\frac{c_T^2 - v^2}{c_s^2 - v^2} \right). \quad (11)$$

In this limit, D becomes $(T/\rho) \partial P/\partial T|_{\rho}$. The differential wind equations, both Newtonian and general-relativistic, are solved in precisely the form above, as a two-point boundary value problem, using a relaxation algorithm described in §3. Note that direct integration of the continuity equation (eq. 1) yields the eigenvalue of the steady-state wind problem, the mass outflow rate $\dot{M} = 4\pi r^2 \rho vy$. In addition, for $\dot{q} = 0$, eqs. (1)–(3) admit a second integral of the flow, the Bernoulli integral. We impose neither as a mathematical constraint in solving the system. Instead, we use the degree to which each is conserved to gauge the accuracy of our converged models. In the Newtonian case, the Bernoulli integral can be expressed by

$$\dot{M} \Delta \left(\epsilon + \frac{1}{2} v^2 + \frac{P}{\rho} - \frac{GM}{r} \right) = \int_{R_\nu}^r d^3 r' \rho \dot{q} = Q(r), \quad (12)$$

where R_ν is the coordinate radius of the protoneutron star surface. In general relativity, with $\dot{q} = 0$, $\gamma h \sqrt{-g_{00}}$ is a constant. Here, γ is the Lorenz factor and h is the specific enthalpy. With a source term, the differential change in neutrino luminosity is given by

$$e^{-2\phi} \frac{\partial}{\partial \mu} (L_\nu e^{2\phi}) = -\dot{q}, \quad (13)$$

where $d\mu/dr = 4\pi r^2 \rho e^\Lambda$ and $ds^2 = -e^{2\phi} dt^2 + e^{2\Lambda} dr^2 + r^2 d\Omega^2$ defines the metric. The total energy deposition rate is then,

$$Q = 4\pi \int_{R_\nu}^\infty dr r^2 \rho q e^\Lambda e^{2\phi}. \quad (14)$$

Using these prescriptions for the Bernoulli integral and the equation for \dot{M} and employing modest radial zoning (2000 points), we typically conserve both to better than 0.1%.

In our solution to the wind problem, we couple the three wind equations in critical form to the differential equation describing the evolution of the electron fraction, Y_e , due to the charged-current electron-type neutrino interactions with free nucleons: $\nu_e n \leftrightarrow e^- p$ and $\bar{\nu}_e p \leftrightarrow e^+ n$. This differential equation does not contain a critical point and can be written as

$$(vy) \frac{dY_e}{dr} = X_n [\Gamma_{\nu_e n} + \Gamma_{e^+ n}] - X_p [\Gamma_{\bar{\nu}_e p} + \Gamma_{e^- p}], \quad (15)$$

where X_n and X_p are the neutron and proton fraction, respectively. The Γ 's are the number rates for emission and absorption, taken from the approximations of Qian & Woosley (1996). The number rate subscripts denote initial-state particles. The asymptotic value of the electron fraction (Y_e^a) is generally determined within ~ 10 km of the protoneutron star surface. Ignoring the details of transport and neutrino decoupling near the neutrinospheres, Y_e^a is determined by both the luminosity ratio $L_{\bar{\nu}_e}/L_{\nu_e}$ and the energy ratio $\langle \varepsilon_{\bar{\nu}_e} \rangle / \langle \varepsilon_{\nu_e} \rangle$, where $\langle \varepsilon_\nu \rangle = \langle E_\nu^2 \rangle / \langle E_\nu \rangle$, and E_ν is the neutrino energy. To rough

(but useful) approximation (Qian et al. 1993; Qian and Woosley 1996),

$$Y_e^a \simeq \frac{\Gamma_{\nu_en}}{\Gamma_{\nu_en} + \Gamma_{\bar{\nu}_ep}} \simeq \left(1 + \frac{L_{\bar{\nu}_e} \langle \varepsilon_{\bar{\nu}_e} \rangle - 2\Delta + 1.2\Delta^2 / \langle \varepsilon_{\bar{\nu}_e} \rangle}{L_{\nu_e} \langle \varepsilon_{\nu_e} \rangle + 2\Delta + 1.2\Delta^2 / \langle \varepsilon_{\nu_e} \rangle} \right)^{-1}, \quad (16)$$

The energy threshold ($\Delta = m_n - m_p \simeq 1.293$ MeV) for the $\bar{\nu}_e$ neutrino absorption process, $\bar{\nu}_e p \rightarrow n e^+$, is manifest in eq. (16). Note the difference in sign on the 2Δ term between numerator and denominator. This implies that simply having $L_{\bar{\nu}_e}/L_{\nu_e} > 1$ and $\langle \varepsilon_{\bar{\nu}_e} \rangle / \langle \varepsilon_{\nu_e} \rangle > 1$ is not sufficient to guarantee $Y_e^a < 0.5$; the magnitudes of $\langle \varepsilon_{\bar{\nu}_e} \rangle$ and $\langle \varepsilon_{\nu_e} \rangle$ are also important. For example, taking $L_{\bar{\nu}_e}/L_{\nu_e} = 1.1$ and $\langle \varepsilon_{\bar{\nu}_e} \rangle / \langle \varepsilon_{\nu_e} \rangle = 13$ MeV/10 MeV gives $Y_e^a \simeq 0.52$. Hence, if $L_{\bar{\nu}_e}$ and L_{ν_e} are correlated with $\langle \varepsilon_{\bar{\nu}_e} \rangle$ and $\langle \varepsilon_{\nu_e} \rangle$, respectively, then even for constant $L_{\bar{\nu}_e}/L_{\nu_e}$ and $\langle \varepsilon_{\bar{\nu}_e} \rangle / \langle \varepsilon_{\nu_e} \rangle$, Y_e^a must increase as the total neutrino luminosity of the protoneutron star decays in time. This phenomenon, which we refer to as the *threshold effect*, is important for the viability of an r -process epoch in protoneutron star winds at late times and low $\langle \varepsilon_{\bar{\nu}_e} \rangle$ and $\langle \varepsilon_{\nu_e} \rangle$. Other possible effects that might bear materially on Y_e^a include the formation of alpha particles from free nucleons (the alpha effect) (Fuller and Meyer 1995; McLaughlin, Fuller, and Wilson 1996), the differential redshift of $\bar{\nu}_e$ neutrinos versus ν_e neutrinos, due to the physical separation of their respective neutrinospheres (Fuller and Qian 1996), and charge conjugation violation (Horowitz and Li 2000).

Coupled to the wind equations and the equation for Y_e evolution is a simple equation of state (EOS) well-suited to the conditions in the neutrino-driven wind ($T \lesssim 5$ MeV, $\rho \lesssim 10^{13}$ g cm $^{-3}$, and $0.0 \lesssim Y_e \lesssim 0.5$). Under these conditions, to good approximation, free neutrons, protons, and alpha particles may be treated as non-relativistic ideal gases. A fully general electron/positron equation of state is employed. Photons are also included. Past wind studies have approximated electrons and positrons as non-degenerate and relativistic. Although $\eta_e (= \mu_e/T)$ divided by π may approach ~ 10 at the protoneutron surface, it drops steeply with the density so that in the main heating region the non-degenerate assumption is justified. In contrast, however, it is important to include the non-relativistic character of the electrons and positrons. For a broad range of protoneutron star characteristics, the temperature drops to ~ 0.5 MeV within $\sim 50 - 100$ km of the neutron star surface. The dynamics and asymptotic character of the wind, including mass outflow rate, asymptotic velocity, and composition can be significantly affected by assuming relativistic electrons and positrons throughout the wind profile. In addition, the important range of matter temperatures for r -process nucleosynthesis occurs for $T(r) \lesssim 0.5$ MeV. Sumiyoshi et al. (2000) have found that using a general electron/positron EOS can decrease the dynamical timescale in the nucleosynthetic region of the wind by as much as a factor of two, a potentially important modification when considering the viability of the neutrino-driven wind as a candidate site for the r -process.

3. NUMERICAL TECHNIQUE

Past numerical studies of steady-state protoneutron star winds have at times been hampered by unphysical boundary conditions and ill-defined numerics not generally suited to the solution of the protoneutron star wind problem.

The solution to the wind equations constitutes an eigenvalue problem. For a given set of protoneutron star characteristics

and boundary conditions, there exists a unique mass outflow rate ($\dot{M} = 4\pi r^2 \rho v$) and critical radius (R_c) where the matter velocity is equal to the local speed of sound ($v(R_c) = c_s$). Although eqs. (5)-(7) are ordinary differential equations, one cannot treat the wind as an initial value problem; the critical point necessitates a two-point boundary value prescription.

Even though shooting methods determine \dot{M} precisely, R_c can remain uncertain (London and Flannery 1982). In addition, although Duncan, Shapiro, & Wasserman (1986) made effective use of this method, they were forced to employ two types of shooting: one for high \dot{M} solutions and another for low \dot{M} solutions. In an effort to circumvent these problems and to construct a robust algorithm with flexible boundary conditions, we solve both the Newtonian and general-relativistic wind equations as a two-point boundary value problem using a relaxation algorithm on an adaptive radial mesh, as described in London & Flannery (1982) (see also Kippenhahn, Weigert, and Hoffmeister 1968; Eggleton 1971; Press et al. 1992).

The relaxation algorithm involves replacing the differential equations with algebraic difference equations at each point on the radial grid. Then, given an initial guess for each variable, at each point, the solution is obtained by iteration. However, because the condition $v(R_c) = c_s$ defines the outer boundary and this point is not known *a priori* - such knowledge would effectively constitute the solution - we follow the procedure of London & Flannery (1982) and introduce a new independent variable q that labels radial mesh points by integers ($q_1 \leq q \leq q_N$). The price paid is three more differential equations:

$$\begin{aligned} \frac{dr}{dq} &= \frac{\psi}{\phi(r)}, \\ \frac{dQ}{dq} &= \psi, \\ \text{and} \quad \frac{d\psi}{dq} &= 0. \end{aligned} \quad (17)$$

In this scheme, r becomes a dependent variable, $Q(r)$ is a mesh spacing function (e.g., $Q(r) = \log r$), ψ is an intermediate variable, and $\phi(r)$ is proportional to the density of mesh points. The system is solved on the mesh of q values. Hence, the outer radial coordinate, at which the $v(R_c) = c_s$ boundary condition is to obtain, adjusts in a Newton-Raphson sense to simultaneously satisfy all boundary conditions. Typically, when we begin a calculation, we start with an initial guess that extends to a radius with Mach number of ~ 0.9 . With each iteration, R_c is adjusted so that the Mach number goes to 1.

We now have three wind equations for $\rho(q)$, $T(q)$, and $v(q)$, three extra differential equations for the mesh algorithm, and the equation for $Y_e(q)$. Seven boundary conditions must then be imposed to close the system. The boundary conditions on the first two of eqs. (17) are simply $r(q_1) = R_\nu$ and $Q(q_1) = \log(R_\nu)$ (for log spacing), where R_ν is the protoneutron star radius. Two more boundary conditions obtain at the critical point. Taking q_N as the outer mesh point, we have that $v(q_N) = c_s$ and we have that the numerator of any of the differential equations for $\rho(r)$, $T(r)$, or $v(r)$ must simultaneously be zero to ensure continuity of the solution through the sonic point. Three additional boundary conditions are required to specify the problem completely. Although simply setting $Y_e(q_1)$, $\rho(q_1)$, and $T(q_1)$ at R_ν is sufficient, we do not use this prescription. Instead, we assume

that the radius of neutrino decoupling coincides with the coordinate radius of the protoneutron star surface. In addition, we assume that this neutrinosphere (R_ν) is the same for all neutrino species: electron (ν_e), anti-electron ($\bar{\nu}_e$), and mu and tau neutrinos (collectively, ν_μ 's). Indeed, as the protoneutron star cools we expect these neutrinospheres to be separated by just tenths of kilometers. As the ν_e neutrinos have the largest net opacity (κ_{ν_e}) of any species, we set an integral boundary condition on their optical depth (τ_{ν_e}):

$$\tau_{\nu_e}(R_\nu) = \int_{R_\nu}^{\infty} \kappa_{\nu_e} \rho dr = \frac{2}{3}. \quad (18)$$

Included in the ν_e opacity are contributions from scattering with free nucleons, scattering on electron/positron pairs, $\nu_e n \rightarrow pe^-$, and alpha scattering. As a second boundary condition, we assume that the net neutrino heating balances the net cooling at R_ν . That is, $\dot{q}(R_\nu) = 0$. Finally, our third boundary condition assumes that the charged-current processes are in equilibrium at the protoneutron star surface. Explicitly,

$$\left. \frac{dY_e}{dr} \right|_{R_\nu} = 0. \quad (19)$$

For a given protoneutron star mass and radius and a set of average neutrino energies and luminosities, we start with a guess for the mass density at the surface of the protoneutron star. We use a two-dimensional Newton-Raphson algorithm to simultaneously satisfy the conditions on \dot{q} and dY_e/dr at R_ν . This determines $T(R_\nu)$ and $Y_e(R_\nu)$ for the first step. At each subsequent iterative step, the relaxation algorithm attempts to satisfy the integral boundary condition on τ_{ν_e} . Effectively, this procedure results in a new $T(R_\nu)$ and $Y_e(R_\nu)$. In this way, we satisfy all boundary conditions simultaneously. Given a good initial guess for the solution (i.e., maximum deviations from convergence in any variable of $\lesssim 20\%$) we obtain a solution in just 5–10 iterations. Once the profile for $R_\nu \leq r \leq R_c$ is obtained, we use l'Hospital's rule to bridge R_c and then integrate to larger radii as an initial value problem using a fourth-order Runge-Kutta scheme. Successfully converged models then serve as an initial guess for the next protoneutron star model with adjacent characteristics (i.e., in mass, radius, or neutrino spectral characteristics).

3.1. Tests of the Code

We do not impose $dM/dr = 0$ or the Bernoulli integral as mathematical constraints on the system. Instead, we use the degree to which these conditions obtain to gauge the precision of our method. Typically, both are conserved to better than 0.1% in both general-relativistic and Newtonian calculations. In addition, as we increase the number of mesh points, the error in both of these quantities decreases significantly.

One may argue that eq. (19) need not hold generally. In fact, we adjusted the code to accept a fixed $Y_e(R_\nu)$ boundary condition to make sure this has no effect on the asymptotic character of the wind. We find that the number rates are large enough at the surface that Y_e is forced from $Y_e(R_\nu)$ to a value such that $dY_e/dr \sim 0$ in the first radial zone with no appreciable effect on any aspect of the wind. For simplicity, then, we have chosen to enforce eq. (19).

Similarly, in a fully dynamical calculation, one would not expect $\dot{q}(R_\nu) = 0$, generally. While this may certainly be true,

in our solution to the steady-state wind we encounter numerical instabilities that preclude solution of the equations with finite $\dot{q}(R_\nu)$. It is difficult to estimate the importance of such an assumption without employing the full machinery of radiation hydrodynamics.

4. THE NEUTRINO HEATING FUNCTION

The neutrino energy deposition rate (\dot{q}) is a sum of contributions from the charged-current ν_e and $\bar{\nu}_e$ neutrino absorption processes, neutrino-electron/positron scattering, neutrino-nucleon scattering, and the process $\nu\bar{\nu} \leftrightarrow e^+e^-$. We describe each in turn.

4.1. The Charged-Current Processes

At the entropies encountered in supernovae ($\lesssim 40$), the charged-current or beta processes ($\nu_e n \leftrightarrow e^- p$ and $\bar{\nu}_e p \leftrightarrow e^+ n$) dominate the opacity and energy exchange for the electron and anti-electron neutrinos. In the protoneutron star wind context, at much higher entropies, we expect these processes to compete with neutrino-electron/positron scattering in the net energy deposition. Ignoring final-state blocking and assuming relativistic electrons and positrons, the charged-current cooling function can be written as

$$C_{cc} \simeq 2.0 \times 10^{18} T^6 \left[X_p \frac{F_5(\eta_e)}{F_5(0)} + X_n \frac{F_5(-\eta_e)}{F_5(0)} \right] \text{ erg g}^{-1} \text{ s}^{-1}, \quad (20)$$

where

$$F_n(y) = \int_0^\infty \frac{x^n}{e^{x-y} + 1} dx$$

are the Fermi integrals, X_n and X_p are the neutron and proton fractions, respectively, T is in MeV, and $\eta_e = \mu_e/T$. The heating rate due to neutrino captures on free nucleons can be written as

$$H_{cc} \simeq 9.3 \times 10^{18} R_{\nu 6}^{-2} \text{ erg g}^{-1} \text{ s}^{-1} \\ \times [X_n L_{\nu_e}^{51} \langle \varepsilon_{\nu_e}^2 \rangle + X_p L_{\bar{\nu}_e}^{51} \langle \varepsilon_{\bar{\nu}_e}^2 \rangle] \Phi^6 \Xi(r), \quad (21)$$

where $R_{\nu 6}$ is the neutrinosphere radius in units of 10^6 cm and both L_ν and $\langle \varepsilon_\nu \rangle$ are defined at R_ν . We separate L_ν and $\langle \varepsilon_\nu \rangle$ in this heating rate and those below. Although L_ν and $\langle \varepsilon_\nu \rangle$ are correlated, L_ν and the tail of the neutrino energy distribution are generally not. We retain L_ν and $\langle \varepsilon_\nu \rangle$ separately so we have the freedom to change them independently. With eqs. (20) and (21), the net energy deposition due to the charged-current processes is then $\dot{q}_{cc} = H_{cc} - C_{cc}$. In eq. (21),

$$\langle \varepsilon_\nu^2 \rangle = \int_{-1}^1 d\mu \int d\varepsilon_\nu \varepsilon_\nu^5 f_\nu \cdot \left[\int_{-1}^1 d\mu \int d\varepsilon_\nu \varepsilon_\nu^3 f_\nu \right]^{-1}, \quad (22)$$

where $\mu (= \cos \theta)$ is the cosine of the zenith angle and f_ν is the neutrino distribution function. Φ accounts for the gravitational redshift of neutrinos from the protoneutron star surface and is given by

$$\Phi = \left(\frac{1 - 2GM/R_\nu c^2}{1 - 2GM/rc^2} \right)^{1/2}. \quad (23)$$

Also present in eq. (21) is the spherical dilution function, $\Xi(r)$, which describes the radial dependence of the neutrino energy

and number densities. In the vacuum approximation, assuming a sharp neutrinosphere,

$$\Xi(r) = 1 - \sqrt{1 - (R_\nu/r)^2/\Phi^2} \quad (24)$$

and is related to the flux factor $\langle\mu\rangle (= F_\nu/J_\nu)$ by $\langle\mu\rangle = R_\nu^2/2\Phi^2\Xi(r)r^2$, where F_ν and J_ν are the neutrino flux and energy density, respectively. In eq. (24), the factor Φ^2 accounts for the bending of null geodesics in a curved spacetime (Cardall and Fuller 1997; Salmonson and Wilson 1999). This effectively increases the neutrino number density a given mass element sees at any radius, thus augmenting the energy deposition. In contrast, since the heating rate for any neutrino interaction is proportional to positive powers of L_ν and $\langle\varepsilon_\nu\rangle$, the gravitational redshift terms which modify these quantities can only decrease the energy deposition rate at a given radius. As pointed out by Cardall & Fuller (1997), the augmentation of \dot{q} by the bending of neutrino trajectories and the degradation of \dot{q} by the gravitational redshift compete as M/R_ν increases, but the latter dominates.

Qian & Woosley (1996), Otsuki et al. (2000), and Wanajo et al. (2000) have employed eq. (24) or its Newtonian analog in their studies of neutrino-driven winds. In an effort to address neutrino decoupling more fully, we compared our wind solutions using this spherical dilution factor to those obtained with an effective $\Xi(r)$ derived from the Monte-Carlo transport results of Janka (1991) who connected $\langle\mu\rangle$ with the density gradient at 10^{10} g cm⁻³ and the curvature of the opacity profile at the radius of decoupling. The difference between the radial dependence of $\langle\mu\rangle$ using this approach and the effective flux factor obtained in a vacuum approximation is significant, as would be expected, only when the atmosphere is sufficiently extended. That is, as the density gradient just exterior to the neutrinosphere goes to infinity, so too should the Monte-Carlo results of Janka (1991) approach the vacuum approximation. Hence, significant deviations from the vacuum approximation only present themselves when the radius of the neutron star is large (~ 20 –40 km) and/or the total neutrino luminosity is very high (i.e., the temperature at R_ν is large). As the protoneutron star cools and the luminosity decreases for a given R_ν , the density gradient becomes steeper (see Fig. 2 below), thus making the vacuum approximation more appropriate. Over the range of models presented here, we have examined the effects of using the Janka (1991) $\langle\mu\rangle$ in order to characterize the spherical dilution of neutrinos for all of the relevant heating processes and find them negligible, particularly for the compact protoneutron star wind models most likely to be important for r -process nucleosynthesis.

We emphasize that this simple comparison is not a complete analysis of the transport effects that might be important in determining $q(r)$. While this result suggests the vacuum approximation is appropriate in our scheme for handling the neutrinospheres and boundary conditions, it says nothing about actual transport effects in the decoupling region.

4.2. Neutrino-Electron/Positron Scattering

At high entropies, electron-positron pairs are produced in abundance. Therefore, neutrino-pair scattering is expected to contribute substantially to the total energy deposition in the protoneutron star wind. The energy transfer associated with a

single neutrino-electron or positron scattering event is well approximated by $\omega_i \simeq (\varepsilon_{\nu_i} - 4T)/2$, where ω is the energy transfer, T is the matter temperature, and ε_{ν_i} is the neutrino energy of species i (Bahcall 1964). We have confirmed this approximation using the thermalization code described in Thompson, Burrows, & Horvath (2000), which employs the fully relativistic structure function formalism of Reddy et al. (1998). The net heating rate due to the interaction of the neutrino fluid with the pair plasma can be approximated by $\dot{q} \simeq cn_e n_{\nu_i} \langle\sigma_{\nu_i e} \omega\rangle$, where n_e and n_{ν_i} are the number density of electrons and neutrinos, respectively, and $\sigma_{\nu_i e}$ is the cross section for scattering. We obtain

$$\dot{q}_{\nu_i e} = \int \omega c \sigma_{\nu_i e} \frac{dn_e}{d\varepsilon_e} d\varepsilon_e \frac{dn_{\nu_i}}{d\varepsilon_{\nu_i}} d\varepsilon_{\nu_i}, \quad (25)$$

where $\sigma_{\nu_i e} (= \kappa_i T \varepsilon_{\nu_i})$ is the cross-section for neutrino scattering on relativistic, non-degenerate electrons (Tubbs and Schramm 1975). $\kappa_i = \sigma_o \Lambda_i / 2m_e^2$ is a neutrino species dependent constant, where m_e is the mass of the electron in MeV, $\sigma_o \simeq 1.71 \times 10^{-44}$ cm², and

$$\Lambda_i = (c_V + c_A)^2 + \frac{1}{3}(c_V - c_A)^2. \quad (26)$$

c_V and c_A are the vector and axial-vector coupling constants for a given neutrino species. We find that the energy deposition rate can be expressed as

$$\dot{q}_{\nu_i e} = \frac{c}{\rho} \left(\frac{T^3}{(\hbar c)^3} \frac{F_2(\eta_e)}{\pi^2} \right) \frac{L_\nu}{4\pi r^2 c \langle\varepsilon_\nu\rangle \langle\mu\rangle} \Phi^2 \text{ erg g}^{-1} \text{ s}^{-1} \\ \times \left[\frac{\kappa}{2} \langle\varepsilon_\nu\rangle \frac{F_4(\eta_\nu)}{F_3(\eta_\nu)} T \left(\langle\varepsilon_\nu\rangle \Phi \frac{F_2(\eta_\nu)}{F_3(\eta_\nu)} - 4T \frac{F_3(\eta_e)}{F_4(\eta_e)} \right) \right]. \quad (27)$$

We drop the subscript i here for brevity. Note that $\langle\mu\rangle (= R_\nu^2/2\Phi^2\Xi(r)r^2)$ contains two powers of the redshift. η_ν is an effective degeneracy parameter obtained from fitting the neutrino distribution function with a Fermi-Dirac distribution with an appropriate T_ν and η_ν (Janka and Hillebrandt 1989). Although we retain the general form here, in the wind calculations presented below we take $\eta_\nu = 0$ for all neutrino species. In eq. (27), the first term in parentheses is the number density of electrons, n_e . Alternatively, with the replacement $\eta_e \rightarrow -\eta_e$, it is the number density of positrons. The next term is the number density of neutrinos, a function of radius, which depends also on the flux factor, $\langle\mu\rangle$. The term in square brackets is the appropriately averaged product of the cross section for scattering and the energy transfer per scattering, $\langle\sigma_{\nu_i e} \omega\rangle$. We retain the form $\dot{q} = cn_e n_{\nu_i} \langle\sigma_{\nu_i e} \omega\rangle$ here for clarity. Note that, for $\eta_\nu = \eta_e = 0$, $\langle\varepsilon_\nu\rangle$ equals $3.15T_\nu$ and the second quantity in parentheses in eq. (27) is simply $(T_\nu - T)$; net heating occurs if $T_\nu > T(r)$ at any r . In order to obtain the contribution to the net heating from neutrino-positron scattering, in addition to the change in η_e , one must also make appropriate changes to Λ_i .

4.3. Neutrino-Nucleon Scattering

The energy transfer associated with a single neutrino-nucleon scattering event is much smaller than that for neutrino-electron scattering. The cross section, however, is much larger. Using our neutrino thermalization code, which solves the Boltzmann equation in an isotropic, homogeneous thermal bath of scatterers, including the full collision term, with Pauli blocking and explicit coupling between all energy bins (Thompson, Burrows, and Horvath 2000), we confirm that the average energy transfer for neutrino-nucleon scattering, in non-degenerate nuclear matter, for neutrino energies below ~ 40 MeV is well approximated by $\omega \simeq \varepsilon_\nu (\varepsilon_\nu - 6T)/m_N$, where m_N is the nucleon

mass in MeV (Tubbs 1979). We derive the heating rate for neutrino-neutron scattering as

$$\dot{q}_{\nu,n} = \frac{cn_n}{\rho} \frac{L_\nu}{4\pi r^2 c \langle \varepsilon_\nu \rangle \langle \mu \rangle} \Phi^4 \text{ erg g}^{-1} \text{ s}^{-1}$$

$$\times \left[\kappa \left(\frac{F_2(\eta_\nu)}{F_3(\eta_\nu)} \langle \varepsilon_\nu \rangle \right)^2 \frac{\langle \varepsilon_\nu \rangle F_6(\eta_\nu)}{m_n F_3(\eta_\nu)} \left(\langle \varepsilon_\nu \rangle \Phi \frac{F_2(\eta_\nu)}{F_3(\eta_\nu)} - 6T \frac{F_5(\eta_e)}{F_6(\eta_e)} \right) \right]. \quad (28)$$

$\kappa = \sigma_o/(16m_e^2)(1+3g_A^2)$ for neutron scattering and $\kappa = \sigma_o/(4m_e^2)[4\sin^4\theta_W - 2\sin^2\theta_W + (1+3g_A^2)/4]$ for neutrino-proton scattering, where $\sin^2\theta_W \simeq 0.231$ and $g_A (\simeq -1.26)$ is the axial-vector coupling constant.

4.4. $\nu_i \bar{\nu}_i \leftrightarrow e^+ e^-$

Cooling due to e^+e^- annihilation, assuming relativistic electrons and positrons, and ignoring Pauli blocking in the final state, can be written as

$$C_{e^+e^- \rightarrow \nu\bar{\nu}} \simeq 1.4 \times 10^{17} \frac{T^9}{\rho_8} f(\eta_e) \text{ ergs g}^{-1} \text{ s}^{-1}, \quad (29)$$

where

$$f(\eta_e) = \frac{F_4(\eta_e)F_3(-\eta_e) + F_4(-\eta_e)F_3(\eta_e)}{2F_4(0)F_3(0)}. \quad (30)$$

ρ_8 is the mass density in units of 10^8 g cm^{-3} and T is in MeV. We employed eq. (29) with and without the η_e dependence and compared it to the results using the fit given in Itoh et al. (1996). Such a modification amounted to no more than a 1-2% change in the entropy, dynamical timescale, total energy deposition, or mass outflow rate.

Much more uncertain than eq. (29) is the heating due to $\nu\bar{\nu} \rightarrow e^+e^-$. The spherical dilution of this process from the neutrinospheres is complicated. For a given flux, the local energy density depends sensitively on $\langle \mu \rangle$, which can only be properly treated by solving the full transport problem. We save such an investigation for a later work. Instead, we compare two approaches. The first is based on the vacuum spherical dilution approximation, written simply as (Qian and Woosley 1996)

$$H \simeq 1.6 \times 10^{19} \frac{\Psi(x)}{\rho_8 R_{\nu_e}^4} \Phi^9 \text{ erg g}^{-1} \text{ s}^{-1}$$

$$\times \left[L_{\bar{\nu}_e}^{51} L_{\nu_e}^{51} (\langle \varepsilon_{\bar{\nu}_e} \rangle + \langle \varepsilon_{\nu_e} \rangle) + \frac{6}{7} (L_{\nu_\mu}^{51})^2 \langle \varepsilon_{\nu_\mu} \rangle \right], \quad (31)$$

where $\Psi(x) = (1-x)^4(x^2+4x+5)$, $x = (1-(R_\nu/r)^2/\Phi^2)^{1/2}$, R_{ν_e} is the neutrinosphere radius in units of 10^6 cm , and $L_{\nu_i}^{51}$ is the neutrino luminosity in units of $10^{51} \text{ erg s}^{-1}$. The redshift term, Φ , appearing in x , accounts for the amplification of this process due to the bending of null geodesics in general relativity as in eq. (24) (Salmonson and Wilson 1999). We compared this approximation to the heating rate obtained by Janka (1991). Because of the extreme nature of the density gradient just exterior to the protoneutron star, we find that the vacuum approximation adequately characterizes the energy deposition. In addition, the fact that there is no obvious way to include the general relativistic effects in the parameterization of $\langle \mu \rangle$ by Janka (1991) led us to employ eq. (31) in the wind models we present here.

4.5. Other Possible Neutrino Processes

We were motivated to consider nucleon-nucleon bremsstrahlung, plasma, and photo-neutrino processes by the sensitivity of the dynamical timescale and asymptotic entropy to changes in the energy deposition profile (see §8.3 and Qian and Woosley 1996). We found that none of these processes contributed significantly. Qian and Fuller (1995a,b) have addressed the possibility that neutrino oscillations may effectively provide an extra energy source, at larger radii, beyond the point where the mass outflow rate is determined. In §8.3, we include an ad hoc energy source to test the sensitivity of our results to changes in $\dot{q}(r)$, but do not address the issue of neutrino oscillations directly.

5. RESULTS: FIDUCIAL MODELS

With a robust and efficient means by which to solve the wind problem, coupled with physical boundary conditions and a well-motivated neutrino heating algorithm we can now survey the protoneutron star wind parameter space.

Supernova and protoneutron star calculations, coupled with observations of neutron star binary systems and our knowledge of the high density nuclear equation of state, place useful limits on the parameter space that protoneutron stars actually inhabit. Particularly, we are interested in a range of protoneutron star masses from 1.2 to 2.0 M_\odot , total neutrino luminosities from 4×10^{52} to $1 \times 10^{51} \text{ erg s}^{-1}$, average neutrino energies as high as 35 MeV for ν_μ neutrinos and 15-20 MeV for ν_e and $\bar{\nu}_e$ neutrinos with $\langle \varepsilon_{\nu_e} \rangle < \langle \varepsilon_{\bar{\nu}_e} \rangle < \langle \varepsilon_{\nu_\mu} \rangle$, and a range of neutron star radii from 20 km to perhaps 9 km.

Our main goal in this section is to map the possible protoneutron star wind parameter space, taking as input the physical ranges specified above. In what follows, we present the basic structure of the wind and identify some of the systematics we can use to assess this site as a candidate for r -process nucleosynthesis. Particularly, we include a discussion of the dynamical timescale, the electron fraction, and the asymptotic entropy. In identifying some of the approximate power law relations which characterize the wind, we refer to *low* and *high* total neutrino luminosities, with *low* denoting $\lesssim 10^{52} \text{ erg s}^{-1}$ and *high* meaning $\gtrsim 10^{52} \text{ erg s}^{-1}$. We write these power laws in terms of L_ν and $\langle \varepsilon_\nu \rangle$. These stand for a representative luminosity and a representative average energy, respectively. That is, we take $L_{\bar{\nu}_e}/L_{\nu_e}$, $L_{\bar{\nu}_e}/L_{\nu_\mu}$, $\langle \varepsilon_{\bar{\nu}_e} \rangle / \langle \varepsilon_{\nu_e} \rangle$, and $\langle \varepsilon_{\bar{\nu}_e} \rangle / \langle \varepsilon_{\nu_\mu} \rangle$ as constant.

We employ the notation L_ν^{51} to refer to luminosities in units of $10^{51} \text{ erg s}^{-1}$. All neutrino luminosities quoted throughout this paper are local quantities at the neutron star surface. The luminosity at infinity can be obtained from the luminosities quoted here by multiplying the local luminosity by two powers of the gravitational redshift (eq. 23). For example, taking $M = 1.4 \text{ M}_\odot$ and $R_\nu = 10 \text{ km}$, $\Phi^2 \simeq 0.58$. In order to keep track of our models, we use the $\bar{\nu}_e$ neutrino luminosity ($L_{\bar{\nu}_e}$) to label each individual model. The total luminosity can then be obtained from the ratios $L_{\bar{\nu}_e}/L_{\nu_e}$ and $L_{\bar{\nu}_e}/L_{\nu_\mu}$. Finally, in our expressions for \dot{q} we included η_{ν_i} terms for completeness. In what follows, we take $\eta_{\nu_e} = \eta_{\bar{\nu}_e} = \eta_{\nu_\mu} = 0$. For an assessment of this assumption, see Janka & Hillebrandt (1989) and Myra & Burrows (1990).

5.1. The Structure of Neutrino-Driven Winds

Figures 1, 2, and 3 show the velocity, mass density, and temperature as a function of radius for eight different neutrino luminosities. For these models, R_ν is 10 km and the neutron star gravitational mass is $1.4 M_\odot$. The average neutrino energies were set at $\langle \varepsilon_{\nu_e} \rangle = 11$ MeV, $\langle \varepsilon_{\bar{\nu}_e} \rangle = 14$ MeV, and $\langle \varepsilon_{\nu_\mu} \rangle = 23$ MeV for the highest luminosity. For each subsequent luminosity, the average energies were decreased according to $\langle \varepsilon_\nu \rangle \propto L_\nu^{1/4}$. The luminosities were held in the ratios $L_{\bar{\nu}_e}/L_{\nu_e} = 1.3$ and $L_{\bar{\nu}_e}/L_{\nu_\mu} = 1.4$. In these figures, critical points ($v = c_s$) are shown as dots. Table 1 lists the global properties of each of these models, including the integrated energy deposition rate, Q (eq. 14), and the mechanical luminosity or hydrodynamical power, $P_{\text{mech}} = \dot{M} v_a^2 / 2$, where v_a is the asymptotic velocity. In addition, we include the asymptotic entropy s_a and dynamical timescale defined as the e -folding time of the density at $T = 0.5$ MeV:

$$\tau_\rho = \frac{1}{v y} \left| \frac{1}{\rho} \frac{\partial \rho}{\partial r} \right|^{-1}. \quad (32)$$

Figure 1 shows clearly that even relatively close to the neutron star ($r \sim 400$ km) the flow is not homologous (i.e., v is not proportional to r). At much smaller radii, however, in the heating region ($r \lesssim 60$ km, compare with Fig. 4) the flow is homologous with $v \propto L_\nu r$. We have found that simple parameterizations of $v(r)$, particularly for low neutrino luminosities, are not straightforward. Although not readily apparent, the asymptotic velocity (v_a) is a power law in L_ν . For high L_ν^{tot} , $v_a \propto L_\nu^{0.3}$. For low L_ν , the index is ~ 0.46 . The critical radius (R_c) also increases as a power of luminosity for low L_ν . For $M = 1.4 M_\odot$, the index is ~ 0.95 , while for $M = 2.0 M_\odot$, $R_c \propto L_\nu^{-0.85}$. Note that if the protoneutron star cools as $L_\nu \propto t^{-0.9}$ then we should expect R_c to grow linearly with time, implying that at late times the velocity of the critical point away from the neutron star is approximately constant.

The stiff nature of the wind equations is manifest in Fig. 2. The inset shows that ρ drops by more than four orders of magnitude in just 1-3 km, before the neutrino heating rate reaches a maximum. Figure 4 shows the total specific heating rate for each of the eight fiducial wind models. Note that the maximum in \dot{q} occurs very close to the protoneutron star surface and that the position of this maximum is not a function of L_ν . At $r \sim 12$ km the density gradient changes dramatically, as the slow moving material in this inner atmosphere accelerates to infinity. Concomitant with this change in $\rho(r)$ and the peak in \dot{q} is a rise in T and most of the entropy production. Figure 5 shows the entropy as a function of radius. Note that the entropy quickly comes to within a few percent of its asymptotic value (s_a). We find that s_a is proportional to $L_\nu^{-0.24}$ for all luminosities, for $1.4 M_\odot$. For $M = 2.0 M_\odot$, s_a is proportional to $L_\nu^{-0.25}$. As L_ν decreases, the gradients in ρ , T , and the entropy near R_ν become larger. Inspection of Fig. 3 shows that the 0.1 MeV $\lesssim T \lesssim 0.5$ MeV region where the r -process (and preceding α -process) might take place, lies between 50 km and 500 km for $L_{\bar{\nu}_e}^{51} = 8.0$ and between 25 km and 150 km for $L_{\bar{\nu}_e}^{51} = 1.0$. Importantly, Fig. 1 shows that the wind is still accelerating significantly at these radii. This calls into question the assumption of a constant velocity outflow used by many r -process modelers (e.g., Meyer and Brown 1997).

Figure 6 shows a breakdown of the total energy deposition into its separate components for the $L_{\bar{\nu}_e}^{51} = 8.0$ fiducial model.

All of the heating processes conspire to give $\dot{q}(R_\nu) = 0$, in accordance with our boundary condition. At the surface, the charged-current heating rate (\dot{q}_{cc}) provides net cooling, which balances heating from neutrino-nucleon scattering ($\dot{q}_{\nu N}$). \dot{q}_{cc} generally dominates the other heating processes in the models we consider here. Note that heating due to neutrino-electron/positron scattering ($\dot{q}_{\nu e}$) does not contribute as significantly as is indicated by Qian & Woosley (1996) and Otsuki et al. (2000), because of their simplifying assumption that the energy transfer per scattering is $\sim \varepsilon_\nu/2$ instead of $\sim (\varepsilon_\nu - 4T)/2$ (§4.2). Comparing Fig. 6 with Fig. 7, we can see that the drop in \dot{q}_{cc} at $r \simeq 35$ km is due to the formation of α particles. As the luminosity decreases this transition region moves in, so that for $L_{\bar{\nu}_e}^{51} = 0.60$, $\dot{q}_{cc} \rightarrow 0$ near $r \sim 22$ km. As the ratio of M/R_ν increases, the heating rate due to $\nu_i \bar{\nu}_i \rightarrow e^+ e^-$ ($\dot{q}_{\nu \bar{\nu}}$) increases substantially relative to both $\dot{q}_{\nu e}$ and \dot{q}_{cc} . In fact, for $M/R_\nu = 2.0 M_\odot/10$ km, the peak in $\dot{q}_{\nu \bar{\nu}}$ is actually slightly higher than that for $\dot{q}_{\nu e}$. However, \dot{q}_{cc} still dominates heating at the peak in \dot{q}_{tot} by a factor of ~ 1.5 . Note that an increase in L_{ν_μ} or $\langle \varepsilon_{\nu_\mu} \rangle$ increases the importance of $\dot{q}_{\nu e}$ and $\dot{q}_{\nu \bar{\nu}}$ relative to \dot{q}_{cc} . In particular, this increases the energy deposition at larger radii. We explore some of these effects on the asymptotic character of the wind in §8.3.

Qian & Woosley (1996) found that $\dot{M} \propto L_\nu^{2.5} M^{-2}$ for Newtonian gravity. We find that the index of this power law in L_ν is slightly decreased in general relativity to 2.4–2.5, but that the dependence on M is stronger; \dot{M} is approximately proportional to $M^{-3.1}$ for high luminosities. The index decreases to –2.7 for low luminosities. For the full range of luminosities and masses considered here, the mass outflow rate in our general-relativistic calculations is approximately a factor of three smaller than in our Newtonian wind models.

Computing the volumetric integral of \dot{q} as in eq. (14) yields the net energy deposition rate, Q (see Table 1). For the heating function we employ in this paper, Q is roughly proportional to $L_\nu^{2.4}$ for all protoneutron star masses and luminosities. The small variations in this power law index compliment the variation in \dot{M} with L_ν so that the ratio Q/\dot{M} varies by less than 2% over the whole range of L_ν for each mass. In all cases $Q/\dot{M} \simeq GM/R_\nu$ to within 10%. Whereas Qian & Woosley (1996) found that $Q \propto M^{-1}$, we find a more stiff dependence on mass; for high L_ν , Q is proportional to $M^{-1.9}$ for $1.4 M_\odot \leq M \leq 1.6 M_\odot$. In addition, we find that their analytic expression for Q consistently underestimates the net energy deposition in our Newtonian models by as much as $\sim 50\%$.

The wind mechanical power P_{mech} is proportional to $L_\nu^{3.4}$ for low L_ν and $M = 1.4 M_\odot$. This index decreases to 3.2 for $M = 2.0 M_\odot$. At high luminosity for all masses, $P_{\text{mech}} \propto L_\nu^{3.2}$. Although the asymptotic velocity is set by the escape velocity from the protoneutron star and therefore increases with increasing M , it does not increase as a power law in general relativity. In fact, it increases more rapidly. Therefore, even though M is approximately proportional to $M^{-2.5}$ at low luminosities, the increase in v_a as M gets large forces P_{mech} to increase.

The efficiency of energy deposition, Q/L_ν^{tot} , ranges from 10^{-3} to 10^{-5} as L_ν decreases. The efficiency of conversion of neutrino energy to hydrodynamical power, $P_{\text{mech}}/L_\nu^{\text{tot}}$, ranges from only 2×10^{-5} to less than 6×10^{-8} for the models considered here. The efficiency for the conversion of net energy deposition to hydrodynamical power, P_{mech}/Q , decreases with luminosity

as $L_\nu^{1.4}$ for $1.4 M_\odot$ with $P_{\text{mech}}/Q \simeq 2.4 \times 10^{-3}$ for $L_{\bar{\nu}_e}^{51} = 0.6$. This means that almost all of the net energy deposition goes into overcoming the gravitational potential. The excess energy, manifest at infinity as the mechanical power, is very small in comparison with Q . These quantities may be potentially important if the wind is to emerge and escape to infinity in the expanding supernova envelope.

5.2. The Effects of General Relativity

Over the range of masses presented here, we find significant enhancements in the entropy per baryon using the full general-relativistic framework. Over a broad range of luminosities for the $1.4 M_\odot$ protoneutron star we find that s_a is 25–30 units less in our Newtonian calculations than in our analogous general-relativistic calculations. Typical reductions in \dot{M} and Q are of order a factor of three and two, respectively. These differences were anticipated by Qian & Woosley (1996) and Cardall & Fuller (1997) and more recently realized in the wind calculations of Otsuki et al. (2000). As the latter showed, the general-relativistic effects on s_a are much more the result of using the general-relativistic hydrodynamic formulation than of incorporating the general-relativistic corrections to \dot{q} expressed in eqs. (23) and (24). The inclusion of general relativity in the hydrodynamics makes the structure of the protoneutron star more compact than in a Newtonian description. This makes the temperature and density gradients steeper just exterior to R_ν , and particularly in the heating region. Although dT/dr decreases rapidly, $d\rho/dr$ drops much faster. This effectively increases the specific energy deposition per unit mass and the entropy is enhanced significantly.

For comparison, we calculated several wind models with eqs. (5)–(7) that included the enhancement to \dot{q} due to the bending of null geodesics, but did not include any redshift factors on L_ν or $\langle \varepsilon_\nu \rangle$. For the $1.4 M_\odot$ model with $L_{\bar{\nu}_e}^{51} = 8.0$ (see Table 1) this change nearly doubled both Q and \dot{M} , while decreasing τ_ρ from 3.68 to 1.95 ms. Although more heating occurred at larger radii, the peak in \dot{q} also increased so as to offset any potential gain in s_a . The net enhancement was just 6 units in entropy. Conversely, keeping all the redshift terms and eliminating Φ from $\Xi(r)$ in eq. (24) increased τ_ρ by more than 30% and left s_a virtually unchanged.

Because the bending of null geodesics increases the net energy deposition close to the neutron star and the redshift terms act to decrease energy deposition over the whole profile, it is clear from this comparison that only an increase in $\dot{q}(r)$ that does not significantly increase Q can have large effects on s_a (see §8.3 and Qian and Woosley 1996).

5.3. The Electron Fraction

Figure 7 shows the evolution of the neutron (X_n), proton (X_p), alpha (X_α), and electron fraction (Y_e) as a function of radius for the $L_{\bar{\nu}_e}^{51} = 8.0$ fiducial model (Table 1 and Figs. 1–6). The electron fraction profile is computed using eq. (15), solved simultaneously with the wind equations. In computing the wind solutions we assume nuclear statistical equilibrium between free nucleons and alpha particles. Y_e comes to within a few percent of its asymptotic value (Y_e^a) in just the first five kilometers. This quick evolution is due primarily to the low matter velocities in the inner region. For $L_{\bar{\nu}_e}/L_{\nu_e} = 8/6.15$ and $\langle \varepsilon_{\bar{\nu}_e} \rangle / \langle \varepsilon_{\nu_e} \rangle = 14/11$,

eq. (16) predicts that $Y_e^a \simeq 0.478$. Solving the differential equation we find remarkable agreement: $Y_e \simeq 0.477$ at $r = 20$ km. Just beyond this, for $r \gtrsim 30$ km, free nucleons form α particles and Y_e rises slightly as X_α increases until $Y_e = 0.485$ at $r \simeq 150$ km. This is the α effect, whose import in this context was first noted by Fuller & Meyer (1995) and McLaughlin, Fuller, & Wilson (1996). The magnitude here is only of order 1%. For $Y_e^a < 0.5$, we find generally that the magnitude of the α effect increases as the luminosity decreases for a given R_ν . In addition, for models in which $L_{\bar{\nu}_e}/L_{\nu_e}$ and $\langle \varepsilon_{\bar{\nu}_e} \rangle / \langle \varepsilon_{\nu_e} \rangle$ are larger, and, hence, Y_e^a is naively lower (à la eq. 16), the magnitude of the α effect is also enhanced. However, for a reasonable range of $L_{\bar{\nu}_e}/L_{\nu_e}$ and $\langle \varepsilon_{\bar{\nu}_e} \rangle / \langle \varepsilon_{\nu_e} \rangle$ as well as total neutrino luminosities, the α effect never increases Y_e^a by more than $\sim 10\%$. That is, if $Y_e = 0.40$ before α particle formation, we find that the α effect increases Y_e to no more than approximately 0.44.

Since in these fiducial models we decrease the average neutrino energies with luminosity, the threshold effect in the charged-current reactions, manifest in eq. (16) by the neutron/proton mass difference (Δ), becomes important. Despite the fact that $L_{\bar{\nu}_e}/L_{\nu_e}$ and $\langle \varepsilon_{\bar{\nu}_e} \rangle / \langle \varepsilon_{\nu_e} \rangle$ are maintained as above, Y_e^a eventually becomes greater than 0.5. As Y_e^a becomes much larger (~ 0.52), it experiences what might also be termed an α effect: because an α particle has $Y_e = Z/A = 0.50$, the onset of X_α formation decreases Y_e^a .

5.4. The Dynamical Timescale

In discussing our results, in order to make an apposite comparison with previous studies, we quote τ_ρ (eq. 32) at $T = 0.5$ MeV. However, using such a scale to characterize the nature of the resulting nucleosynthesis is suspect. Figure 8 shows τ_ρ as a function of radius for the wind models presented in Figs. 1–5. The dots on each line of constant neutrino luminosity mark the range $0.5 \text{ MeV} \gtrsim T(r) \gtrsim 0.1 \text{ MeV}$, the temperature range relevant for neutron-capture nucleosynthesis. Although the r -process may continue at temperatures well below 0.1 MeV, we include these dots to guide the eye. The dynamical timescale of the wind, or the expansion timescale, has been defined in several different ways by many researchers. No clear consensus exists. Cardall & Fuller (1997) defined their dynamical timescale as the e -folding time of the temperature at $T = 0.5$ MeV. Hoffman, Woosley, & Qian (1997) defined their dynamical timescale in the same way, but then used an expansion timescale (1.28 times the dynamical time) to discuss their results. Qian & Woosley (1996) and Freiburghaus et al. (1999) used the ratio r/v at $T = 0.5$ MeV to characterize the expansion. Finally, Meyer & Brown (1997) connect the e -folding time of the density with their expansion timescale, $r/2v$, by using the equation for \dot{M} and dropping the acceleration term. With these assumptions, they obtain

$$\tau_\rho^{\text{MB}}(t) = \tau_0 \left(1 + \frac{t}{2\tau_0} \right), \quad (33)$$

where t is the time on a Lagrangean mass element in the flow. Figure 8 shows clearly that any simple parameterization of the dynamical time, using any definition, is an oversimplification. For $L_{\bar{\nu}_e}^{51} = 8$, τ_ρ increases by a factor of three over this range of temperatures. Equation (33) captures the increase of τ_ρ with radius for high luminosities, but overestimates the slope by about a factor of two. At low luminosities, of course, eq. (33) does not capture $\tau_\rho(t)$ at all. At these luminosities, the dynamical

timescale actually decreases over this range of temperatures. This arises because a region of positive curvature in the $v(r)$ profile of Fig. 1 develops between 40 km and 200 km at low luminosities. This observation simply underscores the danger in considering a single dynamical time that is meant to characterize an actual wind profile.

Figure 9 shows tracks of constant mass in the plane of s_a versus τ_ρ for luminosities from $L_{\bar{\nu}_e}^{51} = 8.0$ to $L_{\bar{\nu}_e}^{51} = 0.70$, for $R_\nu = 10$ km. Although the indices vary slightly for different masses, $s_a \propto L_\nu^{-0.25}$ and $\tau_\rho \propto L_\nu^{-1.4}$, so that s_a is approximately proportional to $\tau_\rho^{0.2}$. One can imagine that these curves represent evolutionary cooling tracks in time in the space of s_a and τ_ρ for constant R_ν and M . Simple extrapolation of this power law allows one to estimate at what τ_ρ a given entropy might obtain, for a given mass and neutron star radius. For example, the $1.4 M_\odot$ trajectory in Fig. 9 will not reach $s_a \simeq 200$ until $\tau_\rho \simeq 0.4$ seconds. The corresponding neutrino luminosity at this point is $L_{\bar{\nu}_e}^{51} \simeq 0.22$. Knowing that $\dot{M} \propto L_\nu^{2.4}$ allows one to estimate the mass outflow rate as $\dot{M} \simeq 1.8 \times 10^{-8} M_\odot \text{ s}^{-1}$. These simple power laws and a knowledge of how L_ν might behave in time allow us to put powerful constraints on the likely wind epoch of r -process nucleosynthesis, as we demonstrate in §6.

Wanajo et al. (2000) found that their dynamical timescale saturated at high neutrino luminosities near $2 - 3 \times 10^{52} \text{ erg s}^{-1}$. This conclusion is an artifact of their definition for the dynamical timescale and their numerical approach to the wind problem. Our solution shows that for constant average neutrino energies, even up to $L_\nu^{\text{tot}} \simeq 8 \times 10^{52} \text{ erg s}^{-1}$, τ_ρ continues to decrease, roughly as $\tau_\rho \propto L_\nu^{-0.75}$. The entropy also decreases as the luminosity increases; $s_a \propto L_\nu^{-0.15}$. Since these power laws are for constant average neutrino energy, we deduce from the fiducial models that $\tau_\rho \propto L_\nu^{-0.75} \langle \varepsilon_\nu \rangle^{-2.6}$ and $s_a \propto L_\nu^{-0.15} \langle \varepsilon_\nu \rangle^{-0.4}$. These are to be compared with the analytic results of Qian & Woosley (1996) who did not include general-relativistic effects: $\tau_{\text{dyn}} \propto L_\nu^{-1} \langle \varepsilon_\nu \rangle^{-2}$ and $s_a \propto L_\nu^{1/6} \langle \varepsilon_\nu \rangle^{-1/3}$. In addition, although we find that τ_ρ decreases as R_ν decreases, for constant protoneutron star mass, neutrino luminosity, and average neutrino energy, using either the Newtonian or general-relativistic wind equations, we find that τ_ρ is generally 10%–15% shorter in the Newtonian case. This result is owed in part to the fact that the increase in q due to the bending of neutrino trajectories is insufficient to counter the decrease in q caused by gravitational redshift of the neutrino luminosity and energy (Cardall & Fuller 1997). (See Table 1 for a comparison between the Newtonian and general-relativistic calculations for the $1.4 M_\odot$ and $L_{\bar{\nu}_e}^{51} = 8.0$ fiducial model.)

5.5. The Steady-State Approximation

To conclude this section, we include a few words about the degree to which the protoneutron star wind can be considered quasi-stationary. There are several timescales of importance. The first is τ_d , the timescale for decay of the neutrino luminosity, set by the power-law index δ in the relation $L_\nu \propto t^{-\delta}$: $\tau_d = t/\delta$. The second is the time τ_m for matter to move from R_ν to the critical point R_c , where it loses sonic contact with the rest of the flow. The third relevant timescale is the sound crossing time, τ_s , between R_ν and R_c . τ_s varies from just ~ 10 ms to more than 250 ms over the range of L_ν 's presented here. For low luminosities, $\tau_s \propto L_\nu^{-1.4}$. τ_m is proportional to $L_\nu^{-2.8}$ for all luminosities and varies from 4 seconds to more than 5000

seconds for the same range of L_ν 's. However, these numbers for τ_m are quite deceiving. In our models, due to the exponential density gradient just exterior to R_ν , the matter is effectively trapped for $r \lesssim 12$ km. In fact, for the lowest luminosity cases presented here, the matter velocity for $r \lesssim 10.5$ km can be of order 10 cm s^{-1} . In effect, then, the region shown in the inset in Fig. 2 is an atmosphere in hydrostatic equilibrium from which the wind emerges. From this region the matter would escape on timescales much longer than the total protoneutron star cooling time. If, instead, we redefine τ_m as the time necessary for a Lagrangean mass element to go from the peak of the heating profile (see Fig. 4) at $r \sim 12$ km to R_c , we find that τ_m is of order $\sim 10 \text{ ms}$ for $L_{\bar{\nu}_e}^{51} = 8.0$ and $\tau_m \sim 1 \text{ second}$ for $L_{\bar{\nu}_e}^{51} = 0.5$. The steady-state approximation is only valid if $\tau_m, \tau_s \ll \tau_d$. For example, taking $L_\nu(t) \propto t^{-0.9}$ and high neutrino luminosities, \dot{M} drops 10% in roughly τ_d . At these luminosities, τ_d is approximately 20–30 ms. Although both τ_m and τ_s are less than τ_d , they are not significantly so. We conclude that the steady-state assumption might be reasonably employed, but that caution is warranted.

6. THE EVOLUTION OF PROTONEUTRON STAR WINDS

With the eigenvalue problem solved and some of the systematics in hand, in this section we explore possible evolutionary trajectories using the steady-state solutions. Beyond surveying the entire relevant parameter space, we endeavor to model the whole of the Kelvin-Helmholtz cooling phase, including radial contraction and the simultaneous evolution of the luminosity and average neutrino energy.

Perhaps a second after core bounce, as the wind emerges, the protoneutron star atmosphere will be extended ($R \sim 30 - 50$ km) and perhaps highly luminous ($L_\nu^{\text{tot}} \sim 5 \times 10^{52} \text{ erg s}^{-1}$). As the neutron star cools it will contract quasi-hydrostatically. This may take as many as several seconds, depending upon the nuclear equation of state. The average neutrino energies during contraction may increase, peak near the time at which R_ν settles, and then decrease roughly linearly in time (Pons et al. 1999). The luminosity may decay quasi-exponentially or as a power law in time (Burrows and Lattimer 1986; Burrows 1988; Pons et al. 1999).

Figure 10 shows the luminosity, radius, and average energy as a function of time for our evolutionary models. This picture is merely schematic, but illustrates a representative scenario. In the following discussion we take $L_\nu^{\text{tot}} \propto t^{-0.9}$. A simple rescaling in time can be performed for other power-law indices or exponential luminosity decay. Two possible tracks for the time evolution of $R_\nu(t)$ are shown. The short dashed line is linear contraction such that $R_\nu(t = 0.4 \text{ s}) = 20.3$ km and $R_\nu(t = 1 \text{ s}) = 10$ km. This is the evolutionary model, which we label as ' $R_\nu(t) \propto 1 - at$ '. For comparison, the dot-dashed line has $R_\nu(t)$ proportional to $t^{-1/3}$. This model also has $R_\nu(t = 0.4 \text{ s}) = 20.3$ km. At $t \simeq 3.2$ seconds, $R_\nu = 10$ km. The power $1/3$ was obtained from a rough fit over approximately one second of post-explosion evolution in a supernova model of S. Bruenn. In this calculation the supernova was simulated in one-dimension artificially for a Woosley and Weaver (1995) $15 M_\odot$ progenitor starting from the collapse calculations of Bruenn, De Nisco, & Mezzacappa (2001). We focus on the model with $R_\nu(t) \propto 1 - at$ instead of the model with $R_\nu(t) \propto t^{-1/3}$ because it reaches a more compact configuration

(i.e., maximum M/R_ν) at earlier times, that is, with higher luminosity. As we explore in the next section, large M/R_ν , coupled with high luminosity and/or average neutrino energy gives short dynamical timescales and relatively high entropies, both potentially important for r -process nucleosynthesis in the protoneutron star context.

In order to determine appropriate numbers for the ratios $\langle \varepsilon_{\nu_\mu} \rangle / \langle \varepsilon_{\bar{\nu}_e} \rangle$, $\langle \varepsilon_{\bar{\nu}_e} \rangle / \langle \varepsilon_{\nu_e} \rangle$, $L_{\bar{\nu}_e} / L_{\nu_\mu}$, and $L_{\bar{\nu}_e} / L_{\nu_e}$ we surveyed supernova simulations (e.g., Mayle, Wilson, and Schramm 1987; Burrows, Hayes, and Fryxell 1995; Mezzacappa et al. 2001; Liebendörfer et al. 2001; Bruenn, De Nisco, and Mezzacappa 2001; Rampp and Janka 2000; S. Bruenn 2001, private communication) and protoneutron star cooling calculations (Burrows and Lattimer 1986; Pons et al. 1999; J. Pons 2000, private communication). The common assumption of equipartition in luminosity between the three neutrino species is generally not realized in these calculations. In fact, $L_{\nu_\mu} + L_{\bar{\nu}_\mu} + L_{\nu_\tau} + L_{\bar{\nu}_\tau}$ is usually of order 50–60% of L_ν^{tot} . In addition, the ratio $\langle \varepsilon_{\bar{\nu}_e} \rangle / \langle \varepsilon_{\nu_e} \rangle$ ranges from 1.1 to 1.4 and $L_{\bar{\nu}_e} / L_{\nu_e}$ from 1.0 to 1.4. The ratio of $\langle \varepsilon_{\bar{\nu}_e} \rangle / \langle \varepsilon_{\nu_e} \rangle$ also varies significantly. Like the fiducial models presented in §5, we use $L_{\bar{\nu}_e}$ to index our evolutionary models in this section and set $\langle \varepsilon_{\nu_\mu} \rangle / \langle \varepsilon_{\bar{\nu}_e} \rangle = 1.6$, $\langle \varepsilon_{\bar{\nu}_e} \rangle / \langle \varepsilon_{\nu_e} \rangle = 1.3$, $L_{\bar{\nu}_e} / L_{\nu_\mu} = 1.4$, and $L_{\bar{\nu}_e} / L_{\nu_e} = 1.3$. At any time, all luminosities and average energies can then be computed from Fig. 10. We chose $\langle \varepsilon_{\bar{\nu}_e} \rangle / \langle \varepsilon_{\nu_e} \rangle$ and $L_{\bar{\nu}_e} / L_{\nu_e}$ so as to accord with the literature while also minimizing Y_e^a (eq. 16), this being potentially favorable for r -process nucleosynthesis (but see §8.1). Note that with $\langle \varepsilon_{\bar{\nu}_e} \rangle / \langle \varepsilon_{\nu_e} \rangle = 1.3$ and $L_{\bar{\nu}_e} / L_{\nu_e} = 1.3$ and the magnitude of the average energies set by Fig. 10, $Y_e^a \sim 0.46$ at early times. We feel these numbers are merely representative. We explore potentially important modifications to our prescription in §8.3.

For each point along the evolutionary models represented in Fig. 10 we calculate the steady-state wind solution. We do this for a range of protoneutron star masses from 1.4–2.0 M_\odot . Neutrino luminosity is always quoted as the local neutrino luminosity at the surface of the protoneutron star, not the luminosity at infinity.

6.1. Results: Evolutionary Models

Shown in Fig. 11 are evolutionary trajectories for $M = 1.4$, 1.6 , 1.8 , and $2.0 M_\odot$ in the plane of τ_ρ versus asymptotic entropy, s_a . Note that s_a does not include contributions from β -decays during nucleosynthesis. During r -process nucleosynthesis these processes may increase s_a by $\gtrsim 10$ units, depending on the dynamical timescale (Meyer and Brown 1997). However, because we post-process our wind models to obtain the nucleosynthetic yield and include only alpha particles and free nucleons in the equation of state we employ in solving the eigenvalue problem (see §2), such an entropy increase is not included in s_a . Figure 11 is analogous to Fig. 9, but for changing $R_\nu(t)$, $\langle \varepsilon_\nu \rangle(t)$, and $L_\nu^{\text{tot}}(t)$ using the evolution depicted in Fig. 10. The evolutionary trajectories labelled with ' $R_\nu \propto 1 - at$ ' are solid lines with small dots. For comparison, we also show the evolution for $M = 1.4 M_\odot$ with $R_\nu(t) \propto t^{-1/3}$ as a thin solid line without dots. The small dots on each evolutionary track are separate L_ν s. All tracks start with $L_{\bar{\nu}_e}^{51} = 8.0$. The lowest luminosity shown on this plot is $L_{\bar{\nu}_e}^{51} = 0.4$ for each track. The time evolution for any mass begins with high luminosity, large R_ν , and, hence, low s_a (~ 50 – 70) and moderate τ_ρ (~ 9 ms). As R_ν gets smaller in the first second of evolution, the trajectories with $R_\nu \propto 1 - at$ move to much higher s_a and slightly

smaller τ_ρ before they cease contraction at $R_\nu = 10$ km. The s_a reached at this luminosity is set by M/R_ν , with the $2.0 M_\odot$ model reaching $s_a \simeq 150$. Our evolutionary models contract from ~ 20 km to $R_\nu = 10$ km in approximately 1 second. At this point in the evolution, R_ν is fixed and each track makes a sharp turn toward much longer τ_ρ and only moderately higher s_a . This turnoff point is marked with a large open circle on each track and has $L_{\bar{\nu}_e}^{51} = 3.4$ and $L_\nu^{\text{tot}} = 1.57 \times 10^{52} \text{ erg s}^{-1}$. At this point the trajectories join lines of constant R_ν , like those in Fig. 9. Due to the relatively slow contraction, the model with $R_\nu(t) \propto t^{-1/3}$ never exhibits such a sharp turn in the $s_a - \tau_\rho$ plane and eventually joins the other $1.4 M_\odot$ evolutionary track at $\tau_\rho \sim 0.015$ seconds, corresponding to $t \simeq 3.15$ seconds and $L_{\bar{\nu}_e}^{51} = 1.3$. Note that the turnoff point at $L_{\bar{\nu}_e}^{51} = 3.4$ marks the point of minimum τ_ρ for each model with $R_\nu \propto 1 - at$. Table 2 gives the global properties of our neutrino-driven wind models at $L_{\bar{\nu}_e}^{51} = 8.0$, $L_{\bar{\nu}_e}^{51} = 3.4$, and $L_{\bar{\nu}_e}^{51} = 0.4$, including the asymptotic electron fraction, Y_e^a . For comparison, we also include in Table 2 the model with $R_\nu(t) \propto t^{-1/3}$ at $L_{\bar{\nu}_e}^{51} = 3.4$.

Having solved for \dot{M} at every point along these evolutionary tracks and assuming that $L_\nu(t) \propto t^{-0.9}$, we calculate the total mass ejected in the wind as a function of time:

$$M_{\text{ej}}(t) = \int_0^t \dot{M}(t') dt'. \quad (34)$$

Figure 12 shows this integral for all five of the models presented in Fig. 11. The dashed line shows $M_{\text{ej}}(t)$ for the model with $R_\nu(t) \propto t^{-1/3}$. As one would expect, because of the slower radial contraction of the protoneutron star, this model ejects more matter than the corresponding trajectory with $R_\nu \propto (1 - at)$. In this case, the difference is about 30%. The small dots on each of the solid lines mark $L_\nu(t)$ for each model and correspond to the luminosity points on each track in Fig. 11. The large dots on each line mark $L_{\bar{\nu}_e}^{51} = 3.4$, the luminosity at which each track in Fig. 11 reaches $R_\nu = 10$ km and turns sharply. Note that the $2.0 M_\odot$ model ejects only $\sim 6 \times 10^{-5} M_\odot$ of material, about three times less than the $1.4 M_\odot$ model. Extrapolating the results of Fig. 12 we can compute the total $M_{\text{ej}}^{\text{tot}}$ for $t \rightarrow \infty$. We can then compute, at any time, the mass yet to be ejected by the wind, $\Delta M_{\text{ej}}(t) = M_{\text{ej}}^{\text{tot}} - M_{\text{ej}}(t)$. Figure 13 shows $\Delta M_{\text{ej}}(t)$ versus time for each track in Fig. 11. The lines and dots correspond with those in Fig. 12. In Fig. 11, we plot lines of constant $\log_{10}[\Delta M_{\text{ej}}(t)]$ in units of M_\odot as dashed lines connecting big dots on each of the four evolutionary trajectories with $R_\nu \propto (1 - at)$. The thick dashed line on the far right side of the plot, labelled -6.0 , is the line beyond which, only $10^{-6} M_\odot$ will be ejected.

In the calculations presented here, we have arbitrarily defined the point in time when the wind begins. The absolute magnitude of M_{ej} in Fig. 12 for each model is therefore also arbitrary. Only the ratios of these ejected masses or $\Delta M_{\text{ej}}(t)$ for an individual trajectory are of real import. The -6.0 line in Fig. 11 is of particular significance because if all (or most) supernovae produce r -process elements then the total yield per supernova must be 10^{-5} – $10^{-6} M_\odot$ (e.g., Qian 2000). Therefore, if an r -process epoch is to exist along any of the trajectories shown in Fig. 11, then it must begin at or before the line labelled -6.0 in order to eject sufficient mass. If r -processing begins to the right of this line, less than $10^{-6} M_\odot$ will be ejected. For any $L_\nu(t)$ and $R_\nu(t)$, such a bound must exist. We have explored the position of this boundary for a variety of relationships for $L_\nu(t)$.

Taking reasonable e -folding timescales (τ) and $L_\nu(t) \propto e^{-t/\tau}$ the -6.0 line moves to even shorter τ_ρ . For slower power law decay, the boundary moves to longer τ_ρ . For $M = 1.4 M_\odot$ and $L_\nu(t) \propto t^{-0.8}$ it moves from $\tau_\rho \simeq 0.07$ to $\tau_\rho \simeq 0.085$ seconds. Although the wind may eventually evolve to arbitrarily long dynamical timescales, we conclude that the range of τ_ρ relevant for r -process nucleosynthesis is significantly constrained by the $\log_{10}[\Delta M_{\text{ej}}] = -6$ line in Fig. 11. In fact, this range is smaller than previous calculations suggest. In addition, note that even if a given wind model produces r -process elements, only a fraction of the total mass ejected during that r -processing epoch will be in r -process elements; much of the mass will remain in alpha particles. Conservatively, then, if transonic protoneutron star winds are the primary site for the r -process, this constraint on the amount of mass ejected per supernova implies that the epoch of r -process nucleosynthesis must occur for τ_ρ less than ~ 0.085 seconds.

For this range in τ_ρ , there is also only a relatively small range of s_a available to the transonic protoneutron star wind. As evidenced by the calculations of Takahashi, Witt, & Janka (1994) and Qian & Woosley (1996) and borne out in Fig. 11, s_a as large as $\simeq 400$ is simply outside what can be obtained for reasonable dynamical timescales, even including the effects of general relativity. If we extrapolate the curves shown here to later times (lower luminosities), even the $2.0 M_\odot$ trajectory does not reach 400 until $\tau_\rho \simeq 0.5$ seconds. At this point $\dot{M} \simeq 1.5 \times 10^{-9} M_\odot \text{ s}^{-1}$. If r -processing could occur during these late stages, it would need to persist for many thousands of seconds to yield even $10^{-6} M_\odot$ of ejecta. Moreover, the survey calculations of Hoffman, Woosley, & Qian (1997) and Meyer & Brown (1997) show that with $s_a \sim 400$ and $\tau_\rho \sim 0.5$ seconds, one requires $Y_e^a \lesssim 0.3$ to achieve an appreciable third peak r -process. A Y_e^a this low is extremely unlikely. As the protoneutron star cools, the neutrino luminosity and average neutrino energy will be correlated. Protoneutron star cooling calculations (Burrows and Lattimer 1986; Pons et al. 1999) indicate that the average neutrino energies will fall throughout these late evolutionary stages as the luminosity decreases. As the magnitude of $\langle \varepsilon_{\bar{\nu}_e} \rangle$ and $\langle \varepsilon_{\nu} \rangle$ decrease, the asymptotic electron fraction (eq. 16) must increase on account of the energy threshold for the reaction $\bar{\nu}_e p \rightarrow n e^+$ (the ‘threshold effect’). For the $1.4 M_\odot$ model, these constraints are even more severe. This track reaches $s_a \sim 400$ only when τ_ρ is several seconds and \dot{M} is of order $10^{-11} M_\odot \text{ s}^{-1}$.

Note that for a given mass and τ_ρ , s_a is 10-30 units higher in Fig. 9 than in Fig. 11 owing to the lower average neutrino energies for a given luminosity in our fiducial models (§5) than in the evolutionary models we consider in this section. One might argue that by quickly decreasing $\langle \varepsilon_\nu \rangle$ for all neutrino species with respect to the luminosity that the trajectory would move more quickly to higher s_a , and, hence, be more likely to yield r -process ejecta. While such a change would certainly drive s_a higher, it would also make τ_ρ increase faster, decrease \dot{M} significantly, and the threshold effect would drive Y_e^a higher. Thus, such a modification can only make the constraints tighter.

We conclude that the late-time r -process as obtained in Woosley et al. (1994) is extremely unlikely in the context of a transonic wind. In essence, because s_a is initially set by M/R_ν for a given model, once each trajectory reaches $R_\nu(t) = 10$ km, the wind evolves quickly to much larger τ_ρ and only modestly higher asymptotic entropy. That is, for constant R_ν , s_a

is roughly proportional to $\tau_\rho^{0.2}$. By the time a transonic wind evolves to high entropy, the dynamical timescale is too long and Y_e^a is too high to allow for a robust r -process. The slope of the trajectories in the $s_a - \tau_\rho$ plane shown in Fig. 11 guarantee that if the wind enters a regime of very high entropy it does so with very large τ_ρ and minute M , so as to preclude any significant r -process yield.

Instead, we propose an r -process epoch just a second or two after explosion, coinciding with the end of the protoneutron star contraction phase. In this scenario, the wind moves into an early-time r -processing regime in the $s_a - \tau_\rho$ plane and then out of this regime at later times so that the constraint on M_{ej} is satisfied. With this in mind, the behavior of the wind trajectories during contraction, and particularly the point in each track where τ_ρ is at a minimum ($L_{\bar{\nu}_e}^{51} = 3.4$), is suggestive and tantalizing. As Hoffman, Woosley, & Qian (1997) noted, a small dynamical timescale, even for only moderate entropies, can yield a successful r -process. More recently, Otsuki et al. (2000) have shown that a successful r -process can be realized in this context. For these reasons we turn our attention to an early-time, high luminosity, short- τ_ρ , and modest entropy r -process. For reference, in Fig. 11, we include long dashed lines of constant Y_e , taken from the r -process survey calculations of Meyer & Brown (1997), above and to the left of which, for a given Y_e^a , production of the third r -process peak at $A \sim 195$ is assured. Caution is encouraged in taking these lines too seriously. They were computed along specific T and ρ trajectories for fixed Y_e^a and dynamical timescale, τ^{MB} , given by eq. (33), which overestimates $d\tau/dt$ by roughly a factor of two at these high luminosities (see Fig. 8 and §5.1). These lines are only suggestive.

7. NUCLEOSYNTHESIS IN THE EVOLUTIONARY PROTONEUTRON STAR WIND MODELS

Any successful r -process site must do more than simply produce nuclei with $A \gtrsim 195$. Observations of r -nuclei in ultra metal-poor halo stars (notably, CS22892-052, HD115444, and CS31082-001) show that the abundance pattern for $A \gtrsim 135$ is nearly identical to the scaled solar r -process abundance (Sneeden et al. 1996; Burris et al. 2000; Westin et al. 2000; Hill et al. 2001). Simply producing the platinum peak is no guarantee that the solar abundance distribution is reliably reproduced (Meyer and Brown 1997). In the wind scenario, particularly, one must construct the time-integrated yield as the neutrino luminosity decays and the global wind structure evolves.

For each luminosity point on the $1.4 M_\odot$ evolutionary trajectory with $R_\nu \propto (1 - at)$ in Fig. 11 we obtained a unique \dot{M} and velocity, temperature, and density profile. For each individual profile we compute the nucleosynthetic yield (Y) as a function of the atomic mass, A . With $Y(A)$ and \dot{M} at every point, assuming $L_\nu(t) \propto t^{-0.9}$, we compute the weighted sum to get the total amount of ejected material at each A , $M_{\text{ej}}(A)$. For the $1.4 M_\odot$ model we find no significant nucleosynthesis beyond $A \sim 100$. In fact, most of the mass is concentrated at a peak in Sr, Y, and Zr. Inspecting the yield at each luminosity (time) reveals that when the protoneutron star has contracted to $R_\nu = 10$ km, the point of minimum τ_ρ in Fig. 11 denoted by a large open circle, the nucleosynthetic flow reaches a maximum in A . That is, all the points with $\tau_\rho \gtrsim 0.006$ seconds on the $1.4 M_\odot$ evolutionary track, even though they have higher entropy, produce lower average A ejecta. This can be understood simply: as the

dynamical timescale of the wind gets longer, more seed nuclei are formed. Hence, for a given Y_e^a and s_a , the neutron-to-seed ratio decreases (Hoffman, Woosley, and Qian 1996; Meyer and Brown 1997; Freiburghaus et al. 1999). Therefore, the point of minimum τ_ρ , when M/R_ν reaches a maximum, affords the best possibility for a robust r -process. For all protoneutron star masses, the evolutionary models with $R_\nu \propto (1-at)$ turn sharply at $L_{\bar{\nu}_e}^{51} = 3.4$ and for τ_ρ between 6 and 7 ms. Unfortunately, although the $L_{\bar{\nu}_e}^{51} = 3.4$ point produced the highest average A ejecta of any other luminosity along the $1.4 M_\odot$ track in Fig. 11, the nucleosynthesis did not even proceed to the second abundance peak.

We also calculated the nucleosynthetic yield for the 1.6 , 1.8 , and $2.0 M_\odot$ trajectories at $L_{\bar{\nu}_e}^{51} = 3.4$, assuming that these points of minimum τ_ρ would also yield the highest average A ejecta of any of the points in a given mass trajectory. None successfully generated nucleosynthesis beyond the second r -process abundance peak. Even the $2.0 M_\odot$ model, which has $s_a \simeq 151$ and $\tau_\rho \simeq 0.0068$ seconds for $L_{\bar{\nu}_e}^{51} = 3.4$, did not proceed beyond $A \sim 135$. Hence, for the Y_e^a 's derived and the time evolution we have assumed, we fail to produce viable r -process nucleosynthesis in any of our evolutionary transonic protoneutron star wind models.

8. WHAT IS TO BE DONE?

We have already ruled out the possibility of a late-time r -processing epoch at long dynamical timescales and high entropies ($s_a \gtrsim 400$) using constraints on the amount of material ejected, the slope of the evolutionary tracks in the $s_a - \tau_\rho$ plane, and the inexorable rise in Y_e^a as the protoneutron star cools.

We are left wondering what reasonable modifications might generically yield third-peak r -process nucleosynthesis for a canonical protoneutron star with $1.4 M_\odot$ and $R_\nu = 10$ km. In this section we further explore the viability of the early-time r -process. We consider the likely range of Y_e^a , s_a , and τ_ρ accessible to transonic neutrino-driven winds, and present the physical conditions we require for production of the both the second and third r -process abundance peaks.

8.1. The Asymptotic Electron Fraction: Y_e^a

One might argue that Y_e^a is simply too high in these winds to yield successful nucleosynthesis. There are several important points in this regard. First, our evolutionary models, which failed to produce nucleosynthesis beyond $A \sim 135$, all had $Y_e^a \sim 0.46$ at $L_{\bar{\nu}_e}^{51} = 3.4$. This Y_e^a favors the formation of $A \sim 90$ nuclei and produces many seed nuclei, thus decreasing the neutron-to-seed ratio for a given entropy and dynamical timescale. Second, both Woosley et al. (1994) and Wanajo et al. (2000) obtained unacceptably large over-productions of nuclei near $A \sim 90$ in the early phase of their wind calculations, at high luminosity and low entropy. Third, Hoffman et al. (1996) find that this overproduction problem is solved if $Y_e^a \gtrsim 0.485$. These three points together imply that if the r -process occurs generically in protoneutron star winds then Y_e^a must be either less than 0.40 or greater than 0.48 to avoid the overproduction problem at $A \sim 90$. Naively, it might seem that $Y_e^a \lesssim 0.40$ is favored because this would naturally increase the neutron-to-seed ratio by increasing the number fraction of neutrons. However, there are several reasons why $Y_e^a \gtrsim 0.48$ might actually

be viable. First, for $Y_e^a \gtrsim 0.485$ Hoffman et al. (1996) found that some interesting p -process elements were produced, which were previously unaccounted for (e.g., ^{92}Mo). Second, the most detailed transport studies done to date (Mezzacappa et al. 2001; Liebendörfer et al. 2001; Rampp and Janka 2000) indicate that $\langle \varepsilon_{\bar{\nu}_e} \rangle / \langle \varepsilon_{\nu_e} \rangle \simeq 1.1 - 1.2$ and $L_{\bar{\nu}_e} / L_{\nu_e} \simeq 1.1$. Depending on the magnitude of $\langle \varepsilon_{\bar{\nu}_e} \rangle$ and $\langle \varepsilon_{\nu_e} \rangle$, these numbers put $Y_e^a \gtrsim 0.48$, as per eq. (16). Third, Hoffman, Woosley, & Qian (1997) find that as Y_e^a increases from 0.48 to ~ 0.495 the requisite entropy for third-peak production actually *decreases* for fixed dynamical timescale. The last point implies that having a high Y_e^a might slightly relieve the constraints on s_a set by an early-time, high-luminosity r -process. The fact that some p -process elements might also be produced in a high Y_e^a environment is attractive. Together, we feel that the above points make it plausible that $Y_e^a \gtrsim 0.48$ in protoneutron star winds. Such a conclusion, constrains the three-dimensional space $s_a - \tau_\rho - Y_e^a$ significantly.

Of course, having $Y_e^a \sim 0.30 - 0.35$ might also cure the over-production problem at $A \sim 90$ while increasing the neutron-to-seed ratio dramatically, so as to allow for third-peak production at the entropies and timescales obtained for the $1.4 M_\odot$ evolutionary model in Fig. 11. However, to attain $Y_e^a \lesssim 0.35$ one requires $L_{\bar{\nu}_e} / L_{\nu_e} \gtrsim 1.55$ for $\langle \varepsilon_{\bar{\nu}_e} \rangle / \langle \varepsilon_{\nu_e} \rangle = 20 \text{ MeV}/12 \text{ MeV}$. Such conditions would be extreme in light of the detailed transport calculations carried out to date. However, if Y_e^a does reach values this low in profiles like those in Fig. 11, there are two constraints worth pointing out. The first is that Y_e^a must evolve with the neutrino luminosities and average energies so that very little mass is left to be ejected by the time Y_e^a increases to 0.40 . Otherwise, the same overproduction problems at $A \sim 90$ may occur. The second constraint is that if Y_e^a is sufficiently low to guarantee third-peak production, it must eject not more than $\sim 10^{-5} M_\odot$ of r -process material per supernova.

We conclude that Y_e^a may be $\gtrsim 0.47$ in protoneutron star winds. This follows from the fact that Y_e^a below 0.40 is very unlikely and if Y_e^a is in the range $0.40 - 0.46$, models suffer from overproduction of $A \sim 90$ nuclei. With this in mind, in the next section we consider modifications to our transonic wind models that might increase the entropy or decrease the dynamical timescale.

8.2. Entropy and Dynamical Timescale

One might choose to increase s_a by changing the bulk protoneutron star characteristics. Increasing the ratio M/R_ν increases s_a significantly with only modest decreases in τ_ρ . However, this ratio cannot be increased arbitrarily. $M \gtrsim 1.5 M_\odot$ may be disfavored in light of neutron star binary observations (Arzoumanian 1995) and $R_\nu < 9$ km seems unlikely due to constraints on the high density nuclear equation of state (e.g., Latimer and Prakash 2001). In order to explore this, however, we varied M and R_ν at $L_{\bar{\nu}_e}^{51} = 3.4$ in our evolutionary models with $R_\nu \propto 1-at$. In Table 3, we summarize these results for $M = 1.8 M_\odot$, $1.6 M_\odot$, and $1.4 M_\odot$. These models should be compared with the models with $L_{\bar{\nu}_e}^{51} = 3.4$ in Table 2. Unfortunately, for $Y_e^a \simeq 0.46$ for each model, we did not obtain third-peak r -process nucleosynthesis. Increasing Y_e^a artificially in our nucleosynthesis calculations to 0.48 , the neutron-to-seed ratio stays low and we fail to generate r -process elements beyond the second peak.

Although reasonable increases in M/R_ν are favorable for the

r-process, they are insufficient for strong third-peak nucleosynthesis. Therefore, in an effort to obtain a robust *r*-process in a canonical $1.4 M_{\odot}$, $R_{\nu} = 10$ km protoneutron star, we are only left with the option of modifications to the energy deposition profile.

8.3. Possible Alterations to \dot{q}

Qian & Woosley (1996) showed that an artificial energy source at radii between 20 km and 30 km, beyond the peak in \dot{q} could substantially increase the entropy and decrease the dynamical timescale. In fact, any extra energy source that broadens the energy deposition profile, thus increasing \dot{q} in a region of low mass density, increases s_a and decreases τ_{ρ} .

We noted in §6 the difference in entropy, for a given τ_{ρ} , between the fiducial tracks in Fig. 9 and the evolutionary tracks in Fig. 11. Comparing the $M = 1.6 M_{\odot}$ tracks on both plots, the difference in s_a between the two at $\tau_{\rho} = 0.02$ seconds is ~ 12 units. The fiducial model (with higher s_a) has a total neutrino luminosity almost twice that of the evolutionary model, but its average neutrino energies are more than 35% lower. The increase in entropy is caused by an interplay between the charged-current heating rate (\dot{q}_{cc}) and the neutrino-electron scattering heating rate ($\dot{q}_{\nu e}$). The former is proportional to $L_{\bar{\nu}_e} \langle \varepsilon_{\bar{\nu}_e}^2 \rangle + L_{\nu_e} \langle \varepsilon_{\nu_e}^2 \rangle$, while $\dot{q}_{\nu e}$ is proportional to $\sum_i L_{\nu_i} \langle \varepsilon_{\nu_i} \rangle$. Clearly, for fixed neutrino luminosities, as the average neutrino energy drops, $\dot{q}_{\nu e}$ becomes more important relative to \dot{q}_{cc} . Because $\dot{q}_{cc} \rightarrow 0$ as the alpha fraction increases (see Figs. 6 and 7), the fact that $\dot{q}_{\nu e}$ increases in importance effectively broadens the energy deposition profile, thus increasing the entropy. Although the heating rate due to $\nu_i \bar{\nu}_i$ annihilation peaks close to the protoneutron star surface, it also contributes to the total energy deposition rate at radii larger than where $\dot{q}_{cc} \rightarrow 0$. Because $\dot{q}_{\nu_i \bar{\nu}_i} \propto \sum_i L_{\nu_i}^2 \langle \varepsilon_{\nu_i} \rangle$, for fixed neutrino luminosity and decreasing average neutrino energy, this process also becomes more important relative to \dot{q}_{cc} , thereby enhancing the effect on s_a . Although the total effect here is relatively small, at short τ_{ρ} any increases in s_a are of potential significance. Small average energies coupled with higher luminosities are one way to achieve moderately higher s_a and shorter τ_{ρ} . Note that due to the threshold effect (eq. 16) in the charged-current reactions, if one decreases $\langle \varepsilon_{\bar{\nu}_e} \rangle$ and $\langle \varepsilon_{\nu_e} \rangle$, Y_e^a will increase, and any potential gains in s_a might be mitigated. However, as we discussed in §8.1, Fig. 10 of Hoffman, Woosley, & Qian (1997) shows that the entropy required for third-peak nucleosynthesis actually decreases for high Y_e^a .

Similarly, one might also increase $\langle \varepsilon_{\nu_{\mu}} \rangle$ and $L_{\nu_{\mu}}$ relative to the same quantities for the electron and anti-electron types. Since the ν_{μ} - and ν_{τ} -type neutrinos do not participate in the charged-current reactions, any increase in their luminosity or average energy effectively increases the importance of $\dot{q}_{\nu e}$ and $\dot{q}_{\nu_i \bar{\nu}_i}$ with respect to \dot{q}_{cc} . As we noted in §6, the evolution of luminosity and energy shown in Fig. 10 is only suggestive. For this reason we explored modifications to the ratios $\langle \varepsilon_{\nu_{\mu}} \rangle / \langle \varepsilon_{\bar{\nu}_e} \rangle = 1.6$, $\langle \varepsilon_{\bar{\nu}_e} \rangle / \langle \varepsilon_{\nu_e} \rangle = 1.3$, $L_{\bar{\nu}_e} / L_{\nu_{\mu}} = 1.4$, and $L_{\bar{\nu}_e} / L_{\nu_e} = 1.3$. For our extreme $2.0 M_{\odot}$ evolutionary model with $L_{\bar{\nu}_e}^{51} = 3.4$ (see Table 2 for comparison), we set $L_{\nu_e} = L_{\bar{\nu}_e} = L_{\nu_{\mu}}$ and $\langle \varepsilon_{\nu_e} \rangle = 15$ MeV, $\langle \varepsilon_{\bar{\nu}_e} \rangle = 22$ MeV, and $\langle \varepsilon_{\nu_{\mu}} \rangle = 34$ MeV. This increased Y_e^a from 0.469 to 0.484, increased Q by more than a factor of three, decreased s_a by 17 units to ~ 134 , and decreased τ_{ρ} by 40% to 4.1 ms. These modifications were insufficient to produce third-peak nucleosynthesis.

Following Qian & Woosley (1996), we artificially increased $\dot{q}(r)$ in the region $20 \text{ km} \leq r \leq 50 \text{ km}$ for our $1.4 M_{\odot}$ evolutionary model at $L_{\bar{\nu}_e}^{51} = 3.4$ so that Q (eq. 14) went from 1.21×10^{49} erg s $^{-1}$ to 1.33×10^{49} erg s $^{-1}$, an increase of 10%. Because Q is the volume integral of ρq and ρ is small at these radii ($10^6 - 10^7 \text{ g cm}^{-3}$), \dot{q} must be enhanced substantially in order to affect a 10% change in Q . With this extra energy deposition we found that maximum increases in s_a and decreases in τ_{ρ} , depending on the degree of augmentation of \dot{q} as a function of r , were 17 units and 50%, respectively. \dot{M} increased by just 8%. We made the same sort of modification to the $2.0 M_{\odot}$ model with $L_{\nu_e} = L_{\bar{\nu}_e} = L_{\nu_{\mu}}$ and $\langle \varepsilon_{\nu_e} \rangle = 15$ MeV, $\langle \varepsilon_{\bar{\nu}_e} \rangle = 22$ MeV, and $\langle \varepsilon_{\nu_{\mu}} \rangle = 34$ MeV. In this case, we increased Q by 6% and found that s_a was increased from 134 to 150 and that τ_{ρ} decreased from 4.1 ms to 2.6 ms. That τ_{ρ} can decrease so significantly as a result of $\lesssim 10\%$ changes in Q demonstrates the importance of conducting a full transport study in this context. We save such an investigation for a future work, but emphasize that the shape of the energy deposition profile may be the final arbiter in determining the true potential of this site as the seat of *r*-process nucleosynthesis.

8.4. The Early-Time *r*-Process

Although we have described the general physics of protoneutron star winds, the resulting nucleosynthesis, and modifications to our models that might enhance the wind's entropy and decrease its dynamical timescale, none of the models we have presented so far produces a robust, third-peak *r*-process. However, setting $M = 2.0 M_{\odot}$, $R_{\nu} = 9$ km, $L_{\bar{\nu}_e} = L_{\nu_e} = L_{\nu_{\mu}} = 8.0 \times 10^{51}$ erg s $^{-1}$, and $\langle \varepsilon_{\nu_e} \rangle = 14.5$ MeV, $\langle \varepsilon_{\bar{\nu}_e} \rangle = 22$ MeV, $\langle \varepsilon_{\nu_{\mu}} \rangle = 34$ MeV, and adding an artificial heating source between 20 km and 50 km that increases Q by 4%, we derive a wind with $s_a \simeq 150$, $\tau_{\rho} \simeq 1.3$ ms, and $Y_e^a \sim 0.477$. This extremely compact and luminous protoneutron star yields a wind profile that produces third-peak *r*-process nucleosynthesis. We have found that for $s_a \sim 150$ and $0.47 \lesssim Y_e^a \lesssim 0.495$, we require $\tau_{\rho} \lesssim 1.3$ ms in order to generate a significant $A \sim 195$ yield. These are the necessary conditions we derive from our general-relativistic wind models for an early-time protoneutron star *r*-process epoch. If a wind trajectory, like those in Fig. 11 were to pass into the region $s_a \sim 150$ and $\tau_{\rho} \lesssim 1.3$ ms with Y_e^a less than 0.50, some third-peak material would be produced. Note that Otsuki et al. (2000) attained third-peak nucleosynthesis for similar wind conditions. Artificially setting Y_e^a equal to 0.40, their model with $s_a \sim 140$ and $\tau_{\rho} \sim 1.2$ ms successfully produced abundance peaks at $A \sim 130$ and $A \sim 195$.

Although a full nucleosynthesis survey, using real wind profiles, is required to map the space $100 \lesssim s_a \lesssim 200$, $\tau_{\rho} \lesssim 1.5$ ms, and $0.46 \lesssim Y_e \lesssim 0.50$, we note some features of potential importance for the short τ_{ρ} , early-time *r*-process. First, as we decrease Y_e^a from 0.495 to 0.47, for a given τ_{ρ} and s_a , the neutron-to-seed ratio stays roughly constant. Hence, the ratio of the abundance yield at $A \sim 130$ to that at $A \sim 195$ is relatively insensitive to Y_e^a . Second, *r*-process nucleosynthesis at very short timescales and high electron fractions is possible because the number of seed nuclei formed is very small. As a consequence, we expect the nucleosynthetic yield in this regime to be sensitive to changes in the input nuclear physics and, in particular, the three-body reactions important in seed nuclei formation (e.g., ${}^4\text{He}(\alpha n, \gamma){}^9\text{Be}$; Kajino et al. 2001).

Our requisite conditions for third-peak nucleosynthesis, $\tau_\rho \lesssim 1.3$ ms, $s_a \simeq 150$, and high Y_e^a , disfavor r -process nucleosynthesis generically in neutrino-driven winds from neutron stars with $M = 1.4 M_\odot$. Our results in Table 3 indicate that even for $R_\nu = 8$ km, s_a is 35 units too small and τ_ρ is a factor of about three too long for the r -process to proceed to the third abundance peak. We find these gaps in entropy and timescale very difficult to bridge. For $M = 1.4 M_\odot$ we require $R_\nu \lesssim 6.5$ km to reach this s_a and τ_ρ . It is unlikely that any high-density nuclear equation of state could accommodate such a small radius. Even taking $M = 1.6 M_\odot$ and $R_\nu = 9$ km, without invoking an artificial heating source, we fail to reach $\tau_\rho \lesssim 1.3$ ms and $s_a \simeq 150$. Although the importance of the distribution of energy deposition and extra heating sources should be borne in mind, our unmodified wind models require a very massive and highly luminous protoneutron star with small radius. Indeed, considering the fact that our successful wind models originate from neutron stars with $M \gtrsim 2.0 M_\odot$ and $R_\nu \lesssim 9$ km, we are forced to consider the possibility that the primary site for the r -process is not a protoneutron star at all. A neutrino-driven outflow generated near the event horizon of a black hole might bear many of the characteristics of our successful protoneutron star models. Perhaps very short timescale outflows or jets originating from the compact inner accretion disk created in the collapsar models of MacFadyen & Woosley (1999) attain the necessary conditions for r -process nucleosynthesis. Such outflow models would benefit by being generated in a region with high M/R_ν , without being subject to the constraints imposed on neutron stars by the nuclear equation of state.

9. DISCUSSION

We have constructed a robust and efficient algorithm for solving the neutrino-driven protoneutron star wind problem using both general relativity and Newtonian gravity. We employed physical boundary conditions for the transonic wind, a well-motivated neutrino energy deposition function, and an equation of state suited to this problem. For the first time, we included the differential equation for the evolution of Y_e in radius and the proper sonic point boundary condition. Using this computational tool, we studied the structure and systematics of neutrino-driven winds with an eye toward assessing the suitability of this site for r -process nucleosynthesis. We have examined a wide range of protoneutron star radii, masses, and neutrino spectral characteristics. By positing an expression for $L_\nu^{\text{tot}}(t)$, we have modeled potential contraction and cooling scenarios that might exist in Nature and calculated the total mass ejected for the corresponding evolutionary trajectories. Employing general relativistic hydrodynamics, we find significant enhancements in the asymptotic entropy of the wind, in good agreement with the post-Newtonian models of Qian & Woosley (1996), the analytic approximations of Cardall & Fuller (1997), and the work of Otsuki et al. (2000). In addition, we find that modest modifications to the net energy deposition rate can markedly improve the conditions for r -process nucleosynthesis. Indeed, we feel that changes in the profile of energy deposition represent the most viable alterations to our models, which might lead to robust r -process nucleosynthesis in the protoneutron star context.

Our results indicate that only an early-time epoch of r -process nucleosynthesis at high L_ν , small τ_ρ , and modest entropy is possible. A late-time r -process, at very high entropy ($\gtrsim 300$), long τ_ρ , and low L_ν , is not viable. There are several

components to this argument. As the luminosity of the protoneutron star decays, both the asymptotic entropy and dynamical timescale of the wind increase. The former is conducive to r -process nucleosynthesis. The latter is not. Hence, the inexorable rise in both compete. Fundamentally, for the transonic wind, we find that the asymptotic entropy does not increase fast enough to compensate for the deleterious rise in τ_ρ . In addition, as the luminosity decays and τ_ρ increases, \dot{M} decreases. For example, our $1.4 M_\odot$ evolutionary model only reaches $s_a \sim 300$ when $\dot{M} \sim 5 \times 10^{-10} M_\odot \text{ s}^{-1}$ and $\tau_\rho \sim 5$ seconds. Clearly, even if the r -process could exist under these conditions, such an epoch would have to continue for many thousands of seconds to produce even $10^{-6} M_\odot$ of r -process ejecta. Finally, the continued rise in Y_e^a at late times as $\langle \varepsilon_{\nu_e} \rangle$ and $\langle \varepsilon_{\bar{\nu}_e} \rangle$ decrease (due to the energy threshold for the reaction $\bar{\nu}_e p \rightarrow ne^+$, the *threshold effect*) also argues against a high- s_a , long- τ_ρ r -process.

For these reasons, we conclude that if r -process nucleosynthesis occurs in protoneutron star winds, it must occur at early times, at or just after the moment when R_ν reaches a minimum. Our $1.4 M_\odot$ evolutionary trajectory with $R_\nu \propto 1 - at$ in Fig. 11 does not attain sufficiently high entropies and short timescales for successful third peak r -process nucleosynthesis. We have calculated the nucleosynthetic yield at every luminosity (time) in this trajectory and at no point does the resulting nucleosynthesis go beyond $A \sim 100$. Interestingly, however, we find that the luminosity point that yields the highest average A ejecta corresponds to the point in time where R_ν reaches a minimum. This point is also a minimum in τ_ρ for the trajectory. We calculated the nucleosynthesis at this same luminosity point for each mass in Fig. 11. Even for the $2.0 M_\odot$ model with $s_a \sim 150$, we did not obtain nucleosynthesis beyond the second abundance peak. As evidenced by the survey calculations of Hoffman, Woosley, & Qian (1997) and Meyer & Brown (1997) and the wind calculations of Otsuki et al. (2000), these models are outside a regime of successful third-peak nucleosynthesis. However, in §8.3 we have shown that reasonable modifications to the spectral character of the neutrinos and the energy deposition function might conceivably shorten τ_ρ sufficiently for the r -process to proceed in some of these models. In §8.4, we found that winds with $s_a \simeq 150$, $\tau_\rho \lesssim 1.3$ ms, and $0.47 \lesssim Y_e^a \lesssim 0.495$ can generate third-peak r -process elements.

If transonic protoneutron star winds are the primary site for r -process nucleosynthesis, then a successful r -process wind model must enter this $s_a - \tau_\rho - Y_e^a$ regime. The wind, starting just after re-ignition of the supernova shock, begins with large R_ν and L_ν^{tot} and, hence, low entropy ($s_a \sim 50$) and short dynamical timescales (τ_ρ is several ms). In order to avoid overproduction of $A \sim 90$ nuclei, Y_e^a is high ($\gtrsim 0.48$) during this low entropy contraction phase (see §8.1; Hoffman et al. 1996). As the protoneutron star contracts, it moves to much higher entropy and shorter τ_ρ . Just as R_ν reaches a minimum and the protoneutron star is at its most compact, s_a is sufficiently high (~ 150), and τ_ρ is sufficiently short ($\lesssim 1.3$ ms) to guarantee successful third peak r -process nucleosynthesis. This epoch does not persist. Because R_ν is now constant in time the wind evolves quickly along trajectories like those in Figs. 9 and 11 with $s_a \propto \tau_\rho^{0.2}$ to much longer timescales and only moderately larger s_a . This, coupled with the rise in Y_e^a due to the threshold effect, effectively shuts off the r -process so that no more than $\sim 10^{-5} M_\odot$ is ejected. We emphasize that this scenario requires the wind to move into and then out of an r -processing regime in the space

of $s_a - \tau_\rho - Y_e^a$.

Such a picture is provocative, but not yet convincing. Simply obtaining a wind solution that has proper s_a , τ_ρ , and Y_e^a to guarantee production of the third peak is hardly sufficient to explain the remarkable agreement between the r -element abundances with atomic masses at and beyond barium in ultra-metal-poor halo stars and the observed solar r -process inventory. It is difficult to understand how such a scenario might consistently reproduce the barium abundance, all the lanthanides, the platinum peak, and the actinides (Cayrel et al. 2001; Hill et al. 2001). In addition, while the data for these halo stars show remarkable consistency with the solar abundances above $A \sim 135$, below this mass they are markedly inconsistent and there is significant star-to-star scatter. Perhaps some subset of all supernovae account for the region below $A \sim 135$ and never undergo a vigorous r -process. Perhaps others do obtain the required s_a , τ_ρ , and Y_e^a and account for the full range of nuclides, including the first abundance peak and proceeding to uranium (Wasserburg and Qian 2000; Qian and Wasserburg 2000; Sneden et al. 1996; Burris et al. 2000). As we demonstrate in §6 with our $R_\nu \propto t^{-1/3}$ model, slow radial contraction of the protoneutron star may preclude any significant r -process yield, as the wind would then never enter a regime of short dynamical timescale with $s_a \sim 150$.

The supernova progenitor structure might be important in this regard. The two-dimensional calculations of Burrows, Hayes, & Fryxell (1995) and Janka & Müller (1995) indicate that a transonic protoneutron star wind can form just tenths of seconds after the successful re-ignition of the supernova shock. The pressure of the wind is sufficient for it to emerge into the expanding supernova ejecta. However, Janka & Müller (1995) found that as the supernova shock passes through the Si-O interface in their one-dimensional $15 M_\odot$ progenitor it causes a strong reverse shock that slows the wind expansion from a $v \sim 2 \times 10^9 \text{ cm s}^{-1}$ to a few times 10^8 cm s^{-1} . It is possible that a termination or reverse shock might generally disrupt the transonic wind as it propagates toward the protoneutron star. Exactly how far in radius the reverse shock propagates will be a function of the hydrodynamical power of both the wind and the reverse shock as the neutrino luminosity decays, each being functions of the progenitor structure. With sufficient power, the reverse shock may continue to the sonic point. This would put the whole region between the protoneutron star surface and the supernova shock in sonic contact, thereby converting a transonic wind into a subsonic breeze. We have conducted preliminary hydrodynamical calculations, which suggest this could occur in certain circumstances. Steady-state solutions to the wind problem can also be formulated in this context, but with an outer boundary pressure set by conditions at the supernova shock. Qian & Woosley (1996) explored the effects of an external boundary pressure on their wind models. This increased the wind entropy by just 11 units, but increased the dynamical timescale by more than 60%. Such a change would be detrimental to an early-time, short- τ_ρ r -process. However, it may be that the reverse shock does not have sufficient power to disrupt the wind interior to the sonic point. In the steady-state, across the shock boundary, the velocity will decrease, the density will increase so as to maintain M , and both the temperature and entropy will increase.

In order to test the effects of a termination or reverse shock on the nucleosynthesis, we inserted a shock by hand at a radius

(r_{sh}) of 4000 km in our wind model with $M = 2.0 M_\odot$ and $R_\nu = 9 \text{ km}$ (see §8.4), far outside the sonic point ($r \simeq 180 \text{ km}$). At r_{sh} the matter velocity was $5.1 \times 10^9 \text{ cm s}^{-1}$, ρ was 17 g cm^{-3} , and T was approximately 0.023 MeV. Using the Rankine-Hugoniot shock jump conditions, we estimate that $v \simeq 7v'$, $\rho \simeq \rho'/7$, and $T \sim T'/2$, where unprimed quantities are for the wind just before the shock ($r < r_{\text{sh}}$), and primed quantities are for the flow just after the shock ($r > r_{\text{sh}}$). These conditions increase s_a by about 10 units in the post-shock region and increase τ_ρ significantly, due to the sudden decrease in v . This had subtle, but potentially significant effects on the resulting r -process yield. To appreciate this, one must understand that without the slowing of the fluid trajectory by passage through the reverse shock, the r -process freeze-out in our wind models occurs for temperatures below 0.01 MeV, because only then are beta decays along the r -process path fast enough to compete with the rapid material expansion. By contrast, if the material slows (and reheats) by passage through the shock, the r -process freeze-out happens at higher temperatures, typically near 0.05 MeV. Although the average number of neutrons captured per seed nucleus is the same for the shocked and unshocked (but otherwise identical) trajectories, the distribution of those neutron captures is different. In particular, for the case considered here, the shocked trajectory had a factor of three larger yield at $A \sim 195$. The reason is that, when the trajectory slowed and reheated by shock passage, the nuclear flow changed and allowed more nuclei to leak out of the $N=82$ closed shell and proceed up to $N=126$ ($A \sim 195$) at the expense of flow from the $N=50$ closed shell ($A \sim 80$) to $N=130$. An additional interesting effect was that, unlike the unshocked trajectory, the shocked trajectory showed evidence of formation of a rare-earth element peak at $A \sim 165$. Surman et al. (1997) argued that this peak forms during freeze-out as the r -process path rapidly moves through the $Z \sim 60$, $N \sim 104$ region of somewhat enhanced nuclear stability in the nuclide chart. In the winds we study here, the shocked trajectories favor such a freeze-out while the unshocked trajectories do not. We conclude that the finer details of the r -process abundance curve may depend in interesting ways on the location and strength of a termination or reverse shock.

These hydrodynamical issues are part of the larger question of fallback in Type-II supernovae. It is possible that the most massive supernova progenitors, with their extended hydrogen envelopes and dense core structures, experience significant fallback over timescales much longer than the cooling time (Chevalier 1989; Woosley and Weaver 1995). Even if the wind were able to emerge from the neutron star for 10-20 seconds after explosion, it might not have sufficient power to overcome extended fallback over minutes and hours. Even without a large overlying hydrogen envelope (Type Ib, Ic), the neutrino-driven wind may be hindered by any progenitor with a large inner core and outer core binding energy. Therefore, we speculate that an early-time r -process, unencumbered by fallback or reverse shocks, is most likely in less massive Type-II, -Ib, or -Ic supernova progenitors. Accretion-induced collapse may offer even more potential in this context for a fully developed, early-time transonic wind as, in this case, there is no overlying mantle to impede the wind's emergence (Fryer et al. 1999).

10. CONCLUSIONS

Our major conclusions are the following:

- For a given mass outflow rate, we find a significantly

- shorter dynamical timescale (τ_ρ) than indicated by many previous investigations.
- Because the temperature, density, and velocity gradients often used in defining a dynamical timescale evolve on a mass element as it moves away from the protoneutron star, employing a unique dynamical timescale to characterize the wind is not recommended.
 - For a given protoneutron star radius, the asymptotic entropy (s_a) is proportional to $\tau_\rho^{0.2}$.
 - A late-time, high entropy ($s_a \gtrsim 300$), long timescale neutrino-driven wind, is not a viable astrophysical site for r -process nucleosynthesis. Although the wind may eventually realize very high entropy, the mass outflow rate will be too small and the dynamical timescale too long at such an epoch to account for the galactic r -process abundance.
 - The third-peak r -process elements can be produced in significant abundance in protoneutron star winds only at early times, at modest entropy ($s_a \sim 150$), and very short dynamical timescale ($\tau_\rho \sim 1$ ms).
 - Winds originating from protoneutron stars with mass $1.4 M_\odot$ and radius $R_\nu = 10$ km do not produce elements beyond $A \sim 100$ at any time during wind evolution.
 - We derive that third-peak r -process arises naturally in the context of spherical, transonic protoneutron star winds only in the unlikely case of protoneutron stars with $M \gtrsim 2.0 M_\odot$ and $R_\nu \lesssim 9$ km.
 - Shocks in the protoneutron star wind, exterior to the sonic point, caused by the wind's interaction with the inner supernova can significantly influence the third-peak and rare-earth r -process element abundances.
- All of these conclusions hold for the generally high Y_e 's (0.46-0.49) derived in this work. Only in the unlikely case that Y_e in the wind is $\lesssim 0.35$ are our conclusions dramatically altered. In this case, third-peak r -process nucleosynthesis might be obtained in our transonic models for protoneutron star masses less than $2.0 M_\odot$ and radii greater than 9 km, at early times in the wind evolution. The uncertainty in the spectral characteristics of the electron and anti-electron neutrinos in determining the asymptotic electron fraction during wind formation and evolution is primary on our list of unresolved issues. Others include:
- the character of the energy deposition profile as obtained from detailed neutrino transport in a self-consistent calculation,
 - the high-density nuclear equation of state, which would elucidate the range of protoneutron star masses and radii relevant,
 - the hydrodynamical interaction of the wind and shocks in the expanding post-supernova environment,
 - the effects of rotation and magnetic fields,
 - exactly how, even given successful third-peak nucleosynthesis for a given model, the universality of the observed r -process distribution for $A \gtrsim 135$ can be accounted for generically by the progenitor-dependent parameter space of neutrino-driven winds.

These last points leave the prospect of the r -process in this context an open question. We conclude from this study that if the r -process occurs in protoneutron star winds, it most likely occurs at early times after the preceding supernova, in winds with very short dynamical timescales ($\lesssim 1.3$ ms), moderate entropies (~ 150), and, possibly, high electron fractions ($0.47 \lesssim Y_e^a \lesssim 0.495$). In contrast to the early-time scenario, because protoneutron star winds only enter a high entropy ($s_a \gtrsim 300$) regime with very low \dot{M} ($\lesssim 10^{-9} M_\odot$ s $^{-1}$) and extremely long timescales ($\tau_\rho \gtrsim$ seconds), a late-time r -process is simply not viable. Conditions suitable for an early-time r -process are realized in our models only by very compact protoneutron stars with $M = 2.0 M_\odot$ and $R_\nu \lesssim 9$ km. The conditions necessary for third-peak r -process nucleosynthesis are not realized in neutrino-driven transonic winds from canonical neutron stars with $M = 1.4 M_\odot$ and $R_\nu = 10$ km. In fact, for this neutron star mass, we require $R_\nu \lesssim 6.5$ km. Although such neutron star masses and radii are not entirely excluded by current high density equations of state, such radii seem unlikely to obtain in the early post-supernova phase. The short-timescale jet outflows from the dense inner accretion disk around a black hole formed in the collapsar models of MacFadyen & Woosley (1999) might attain the necessary entropies and timescales for the r -process, since in that context M/R_ν can be significantly larger than in the protoneutron star context. Importantly, it should be noted that we consistently produce r -process nucleosynthesis *below* $A \sim 135$. Perhaps protoneutron stars of canonical mass and radius ($1.4 M_\odot$, 10 km) produce elements in this mass range generically, thus accounting (due to progenitor structure and temporal characteristics of the neutrino spectrum) for the variations in abundance observed in these elements in ultra-metal-poor halo stars.

11. ACKNOWLEDGEMENTS

T. A. T. is supported by a NASA GSRP fellowship. B. S. M. is supported by NASA grant NAG5-4703 and NSF grant AST 98-19877. The authors would like to thank Philip Pinto for helpful discussions and both José Pons and Steven Bruenn for providing useful information from their protoneutron star cooling and supernova calculations, respectively. In addition, we thank George Fuller, Christian Cardall, and Jason Pruet for their comments and critical reading of the text. Wind profiles are available upon request from T. A. T.

REFERENCES

- Arzoumanian, Z. 1995, PhD Thesis, Princeton University
 Bahcall, J. N. 1964, Physical Review, 136, B1164
 Bruenn, S. W., De Nisco, K. R., & Mezzacappa, A. 2001, preprint (astro-ph/0101400)

- Burbidge, E. M., Burbidge, G. R., Fowler, W. A., & Hoyle, F. 1957, Rev. Mod. Phys., 29, 547
 Burris, D. L., Pilachowski, C. A., Armandroff, T. E., Sneden, C., Cowan, J. J., & Roe, H. 2000, ApJ, 544, 302

- Burrows, A. & Lattimer, J. M. 1986, ApJ, 307, 178
- Burrows, A. 1988, ApJ, 334, 891
- Burrows, A., Hayes, J., & Fryxell, B. A. 1995, ApJ, 450, 830
- Cardall, C. Y. & Fuller, G. M. 1997, ApJL, 486, 111
- Chevalier, R. 1989, ApJ, 346, 847
- Cayrel, R., Hill, V., Beers, T. C., Barbuy, B., Spite, M., Spite, F., Plez, B., Andersen, J., Bonifacio, P., Francois, P., Molaro, P., Nordström, B., & Primas, F. 2001, Nature, 409, 691
- Cowan, J. J., Sneden, C., Truran, J. W., & Burris, D. L. 1996, ApJL, 460, 115
- Duncan, R. C., Shapiro, S. L., & Wasserman, I. 1986, ApJ, 309, 141
- Eggleton, P. P. 1971, MNRAS, 151, 351
- Flammang, R. A. 1982, MNRAS, 199, 833
- Freiburghaus, C., Rosswog, S., & Thielemann, F.-K. 1999, ApJL, 525, 121
- Freiburghaus, C., Rembges, J.-F., Rauscher, T., Kolbe, E., Thielemann, F.-K., Kratz, K.-L., Pfeiffer, B., & Cowan, J. J. 1999, ApJ, 516, 381
- Fryer, C. L., Benz, W., Herant, M., & Colgate, S. 1999, ApJ, 516, 892
- Fuller, G. M. & Meyer, B. S. 1995, ApJ, 453, 792
- Fuller, G. M. & Qian, Y.-Z. 1996, Nucl. Phys. A, 606, 167
- Hill, V., Plez, B., Cayrel, R., & Beers, T. C. 2001, proceedings of Astrophysical Ages and Timescales, ASP Conference Series, preprint (astro-ph/0104172)
- Hoffman, R. D., Woosley, S. E., Fuller, G. M., & Meyer, B. S. 1996, ApJ, 460, 478
- Hoffman, R. D., Woosley, S. E., & Qian, Y.-Z. 1997, ApJ, 482, 951
- Horowitz, C. J. & Li, G. 2000, Proceedings of Intersections Conference, Quebec, preprint (astro-ph/0010042)
- Itoh, N., Hayashi, H., Nishikawa, A., & Kohyama, Y. 1996, ApJS, 102, 411
- Janka, H.-Th. & Müller, E. 1995, ApJL, 448, 109
- Janka, H.-T. 1991, A&A, 244, 378
- Janka, H.-Th. & Hillebrandt, W. 1989, AA, 224, 49
- Kajino, T., Otsuki, K., Wanajo, S., Orito, M., & Mathews, G. 2001, to appear in Few-Body Systems Suppl., preprint (astro-ph/0006079)
- Kippenhahn, R., Weigert, A., & Hoffmeister, E. 1968, Meth. Comput. Phys., 7, 129
- Lattimer, J. M. & Prakash, M. 2001, ApJ, 550, 426
- Liebendörfer, M., Mezzacappa, A., Thielemann, F.-K., Messer, O. E. B., Hix, W. R., & Bruenn, S. W. 2000, PRD, submitted, preprint (astro-ph/0006418)
- London, R. A. & Flannery, B. P. 1982, ApJ, 258, 260
- MacFadyen, A. I. & Woosley, S. E. 1999, ApJ, 524, 262
- Mayle, R., Wilson, J. R., & Schramm, D. N. 1987, ApJ, 318, 288
- McLaughlin, G., Fuller, G. M., & Wilson, J. R. 1996, ApJ, 472, 440
- McWilliam, A., Preston, G. W., Sneden, C., & Searle, L. 1995a, AJ, 109, 2757
- McWilliam, A., Preston, G. W., Sneden, C., & Shectman, S. 1995b, AJ, 109, 2757
- Meyer, B. S. & Brown, J. S. 1997, ApJS, 112, 199
- Meyer, B. S., Howard, W. M., Mathews, G. J., Woosley, S. E., & Hoffman, R. D. 1992, ApJ, 399, 656
- Mezzacappa, A., Liebendörfer, M., Messer, O. E. B., Hix, W. R., Thielemann, F.-K., & Bruenn, S. W. 2001, PRL, 86, 1935
- Myra, E. S. and Burrows, A. 1990, ApJ, 364, 222
- Nobili, L., Turolla, R., & Zampieri, L. 1991, ApJ, 383 250
- Otsuki, K., Tagoshi, H., Kajino, T., & Wanajo, S.-Y. 2000, ApJ, 533, 424
- Pons, J. A., Reddy, S., Prakash, M., Lattimer, J. M., & Miralles, J. A. 1999, ApJ, 513, 780
- Press, W. H., Teukolsky, S. A., Vetterling, W. T., & Flannery, B. P. 1992, Numerical Recipes in Fortran 77 (2d Ed.; New York, NY: Cambridge University Press)
- Qian, Y.-Z., Fuller, G. M., Mathews, G. J., Mayle, R. W., Wilson, J. R., Woosley, S. E. 1993, PRL, 71, 1965
- Qian, Y.-Z. 2000, ApJL, 534, 67
- Qian, Y.-Z. & Fuller, G. M. 1995a, PRD, 51, 14, 1479
- Qian, Y.-Z. & Fuller, G. M. 1995b, PRD, 52, 2, 656
- Qian, Y.-Z. & Wasserburg, G. J. 2000, Phys. Reps., 333, 77
- Qian, Y.-Z. & Woosley, S. E. 1996, ApJ, 471, 331
- Rampp, M. & Janka, H.-Th. 2000, ApJL, 539, 33
- Reddy, S., Prakash, M., & Lattimer, J. M. 1998, PRD, 58, 013009
- Rosswog, S., Liebendörfer, M., Thielemann, F.-K., Davies, M., Benz, W., & Piran, T. 1999, A&A, 341, 499
- Salmonson, J. D. & Wilson, J. R. 1999, ApJ, 517, 859
- Sneden, C., McWilliam, A., Preston, G. W., Cowan, J. J., Burris, D. L., & Armsky, B. J. 1996, ApJ, 467, 819
- Sumiyoshi, K., Suzuki, H., Otsuki, K., Teresawa, M., & Yamada, S. 2000, PASJ, 52, 601
- Surman, R., Engel, J., Bennett, J. R., & Meyer, B. S. 1992, PRL, 79, 1809
- Takahashi, K., Witt, J., & Janka, H.-T. 1994, A&A, 286, 857
- Thompson, T. A., Burrows, A., & Horvath, J. E. 2000, PRC, 62, 035802
- Tubbs, D. L. 1979, ApJ, 231, 846
- Tubbs, D. L. & Schramm, D. N. 1975, ApJ, 201, 467
- Wallerstein, G., Iben, I., Parker, P., Boesgaard, A. M., Hale, G. M., Champagne, A. E., Barnes, C. A., Kappeler, F., Smith, V. V., Hoffman, R. D., Timmes, F. X., Sneden, C., Boyd, R. N., Meyer, B. S., & Lambert, D. L. 1997, Rev. Mod. Phys., 69, 995
- Wanajo, S., Kajino, T., Mathews, G. J., & Otsuki, K. 2001, accepted to ApJ
- Wasserburg, G. J. & Qian, Y.-Z. 2000, ApJL, 529, 21
- Westin, J., Sneden, C., Gustafsson, B., & Cowan, J. J. 2000, ApJ, 530, 783
- Woosley, S. E. and Hoffman, R. D. 1992, ApJ, 395, 202
- Woosley, S. E., Wilson, J. R., Mathews G. J., Hoffman, R. D., & Meyer, B. S. 1994, ApJ, 433, 209
- Woosley, S. E. & Weaver, T. A. 1995, ApJS, 101, 181

TABLE 1
FIDUCIAL WIND MODELS: $1.4 M_{\odot}$

$L_{\nu_e}^{51}$	L_{ν}^{tot} (10^{51} erg s $^{-1}$)	\dot{M} (M_{\odot} s $^{-1}$)	Q (10^{48} erg s $^{-1}$)	P_{mech} (10^{48} erg s $^{-1}$)	τ_{ρ} (ms)	s_a
8.0	37.0	9.05×10^{-5}	35.1	0.848	3.68	83.9
8.0 ^a	37.0	2.70×10^{-4}	75.1	2.54	3.28	68.2
7.0	32.4	6.56×10^{-5}	25.1	0.561	4.24	86.4
6.0	27.6	4.47×10^{-5}	17.1	0.346	5.01	89.5
5.0	23.1	2.84×10^{-5}	10.9	0.194	6.14	93.4
4.0	18.5	1.63×10^{-5}	6.28	0.0929	7.93	98.4
3.0	13.9	8.03×10^{-6}	3.09	0.0346	11.29	105.4
2.0	9.25	3.74×10^{-6}	1.14	8.59×10^{-3}	19.19	116.2
1.0	4.63	5.44×10^{-7}	0.211	8.24×10^{-4}	49.54	137.6
0.6	2.78	1.58×10^{-7}	0.062	1.50×10^{-4}	100.9	156.3

^aNewtonian calculation

TABLE 2
EVOLUTIONARY WIND MODELS: $L_{\nu_e}^{51} = 8.0, 3.4$, AND 0.4

Mass (M_{\odot})	$L_{\nu_e}^{51}$	L_{ν}^{tot} (10^{51} erg s $^{-1}$)	R_{ν} (km)	\dot{M} (M_{\odot} s $^{-1}$)	Q (10^{48} erg s $^{-1}$)	P_{mech} (10^{48} erg s $^{-1}$)	τ_{ρ} (ms)	s_a	Y_e^a
2.0	8.0	37.0	20.3	2.19×10^{-4}	53.3	1.27	10.45	67.08	0.467
1.8	8.0	37.0	20.3	3.03×10^{-4}	67.2	1.67	9.87	59.05	0.465
1.6	8.0	37.0	20.3	4.38×10^{-4}	83.8	2.27	9.27	51.39	0.463
1.4	8.0	37.0	20.3	6.69×10^{-4}	108.2	3.25	8.63	44.02	0.460
2.0	3.4	15.7	10.0	9.80×10^{-6}	5.94	0.0826	6.83	151.61	0.469
1.8	3.4	15.7	10.0	1.39×10^{-5}	7.34	0.108	6.78	129.43	0.467
1.6	3.4	15.7	10.0	2.04×10^{-5}	9.29	0.148	6.56	109.70	0.465
1.4	3.4	15.7	10.0	3.14×10^{-5}	12.1	0.213	6.21	91.78	0.462
1.4 ^a	3.4	15.7	14.7	9.03×10^{-4}	21.8	0.424	9.98	64.01	0.457
2.0	0.4	1.85	10.0	1.24×10^{-7}	0.0757	1.97×10^{-4}	75.49	234.20	0.492
1.8	0.4	1.85	10.0	1.72×10^{-7}	0.0923	2.48×10^{-4}	75.21	198.88	0.491
1.6	0.4	1.85	10.0	2.46×10^{-7}	0.114	3.23×10^{-4}	72.92	167.40	0.490
1.4	0.4	1.85	10.0	3.67×10^{-7}	0.144	4.44×10^{-4}	69.14	138.92	0.489

^aThe $1.4 M_{\odot}$ trajectory in Fig. 11 with $R_{\nu} \propto t^{-1/3}$, for $L_{\nu_e}^{51} = 3.4$.

TABLE 3
MODIFIED EVOLUTIONARY WIND MODELS: $L_{\nu_e}^{51} = 3.4$ AND $Y_e^a \simeq 0.46$

Mass (M_{\odot})	L_{ν}^{tot} (10^{51} erg s $^{-1}$)	R_{ν} (km)	\dot{M} (M_{\odot} s $^{-1}$)	Q (10^{48} erg s $^{-1}$)	P_{mech} (10^{48} erg s $^{-1}$)	τ_{ρ} (ms)	s_a
1.8	15.7	9.0	1.01×10^{-5}	6.18	0.092	5.63	146.44
1.6	15.7	9.0	1.48×10^{-5}	7.79	0.122	5.61	122.98
1.4	15.7	9.0	2.29×10^{-5}	10.2	0.174	5.39	102.15
1.4	15.7	8.5	1.94×10^{-5}	9.25	0.157	4.97	108.48
1.4	15.7	8.0	1.62×10^{-5}	8.35	0.141	4.54	115.86

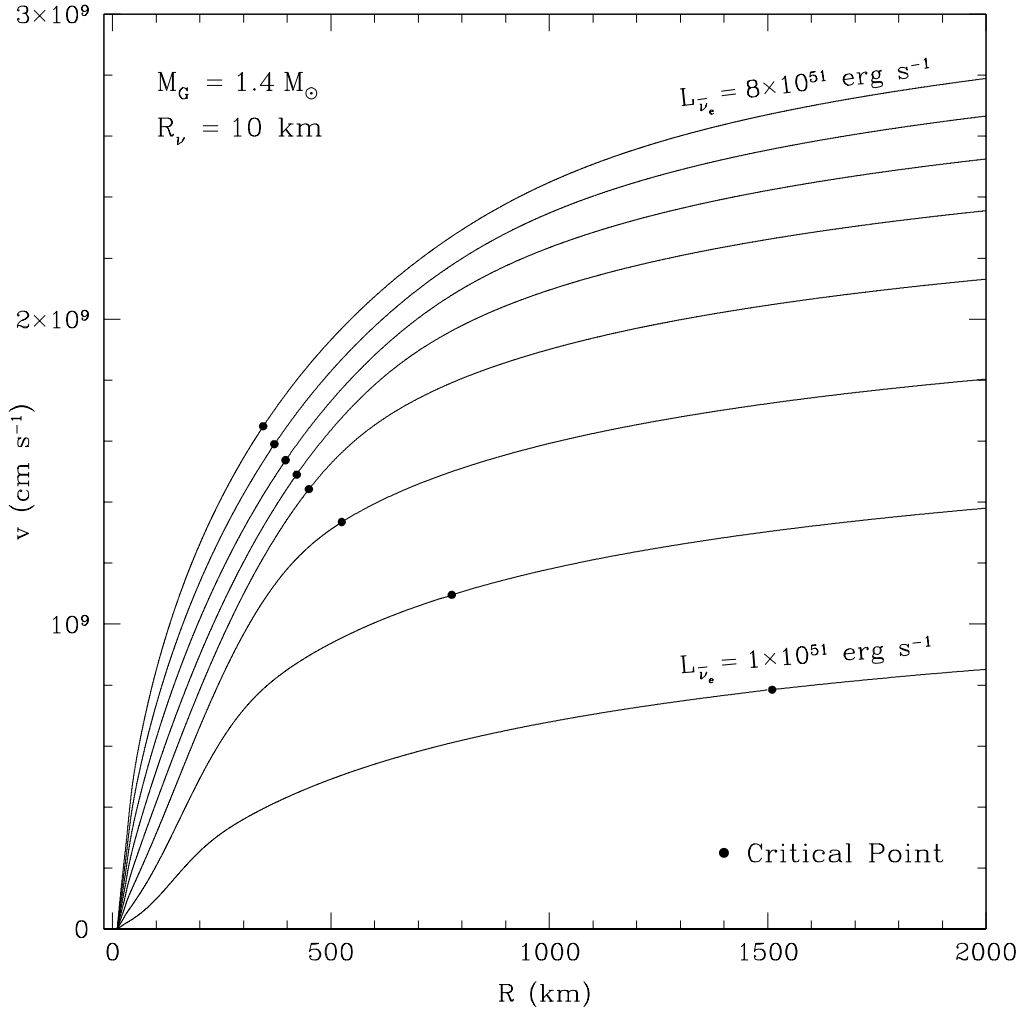


FIG. 1.—Matter velocity (v) in cm s^{-1} as measured in the Schwarzschild frame as a function of radius (R) in km for a $1.4 M_{\odot}$ (gravitational) protoneutron star with $L_{\bar{\nu}_e} = 8, 7, 6, 5, 4, 3, \text{ and } 1 \times 10^{51} \text{ erg s}^{-1}$. For $L_{\bar{\nu}_e} = 8 \times 10^{51} \text{ erg s}^{-1}$, we set $\langle \varepsilon_{\nu_e} \rangle = 11 \text{ MeV}$, $\langle \varepsilon_{\bar{\nu}_e} \rangle = 14 \text{ MeV}$, and $\langle \varepsilon_{\nu_\mu} \rangle = 23 \text{ MeV}$. For each subsequent luminosity, the average neutrino energy for each species was decreased according to $\langle \varepsilon_{\nu} \rangle \propto L_{\nu}^{1/4}$. The luminosities were set in the ratios $L_{\bar{\nu}_e}/L_{\nu_e} = 1.3$ and $L_{\bar{\nu}_e}/L_{\nu_\mu} = 1.4$. The dots mark the critical point for each wind profile, where the matter velocity is equal to the local speed of sound. The neutrinosphere radius is held fixed at 10 km. For all profiles, for $r \lesssim 60 \text{ km}$, the flow is nearly homologous with $v \propto L_{\nu} r$.

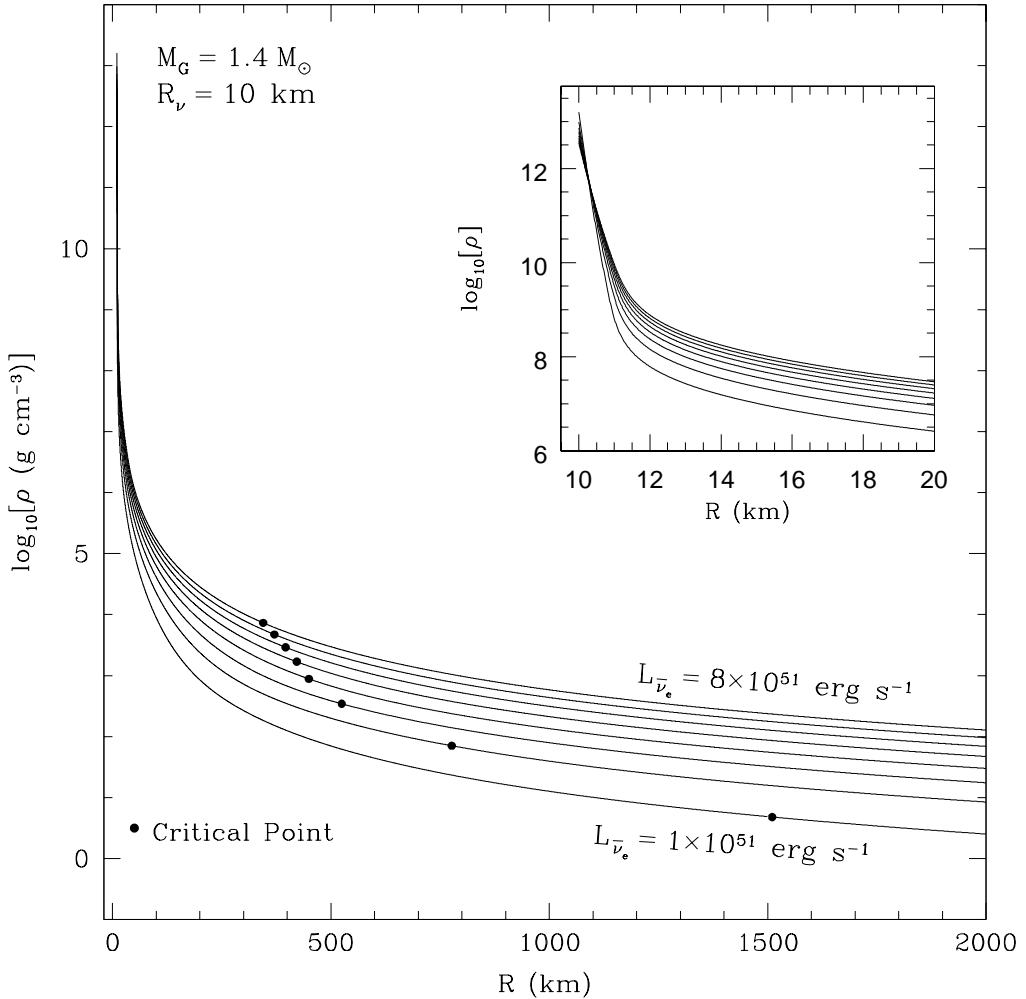


FIG. 2.— \log_{10} of the mass density (ρ) in g cm^{-3} versus radius (R) in km for the same range of neutrino luminosities as in Fig. 1 and for the same protoneutron star characteristics. Dots mark the critical point. The inset shows $\log_{10}\rho$ versus R for the region close to the protoneutron star. Note the steep density gradient, which drops precipitously over as much as five orders of magnitude in just over a kilometer. As the neutrino luminosity decreases, $\rho(R_\nu)$ increases in order to maintain our inner integral boundary condition on the ν_e neutrino optical depth (eq. 18).

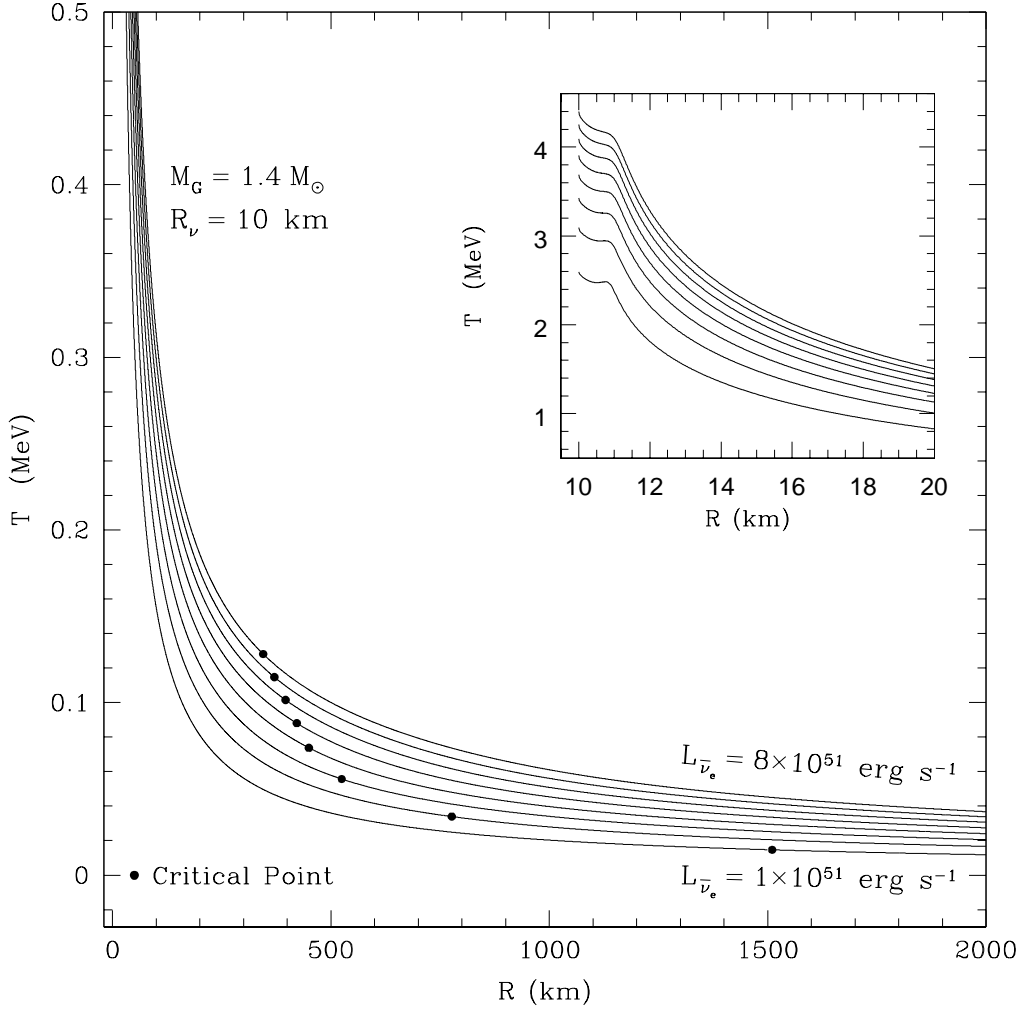


FIG. 3.—Matter temperature (T) in MeV versus radius in km for the same profiles as in Fig. 1. Dots mark the critical point. Note that the important regime of possible r -processing lies between 0.5 MeV and approximately 0.08 MeV, a region extending out to 700 km for the highest luminosities and to less than 200 km for the lowest luminosities shown. Comparing the temperature in this range of radii to those in Fig. 1, it's clear that the assumption of constant outflow velocity (Meyer and Brown 1997) is a poor approximation during nucleosynthesis in neutrino-driven winds. The inset shows the structure of the temperature as a function of radius very close to the neutrinosphere. The bump in T is caused by the onset of heating (compare with Fig. 4).

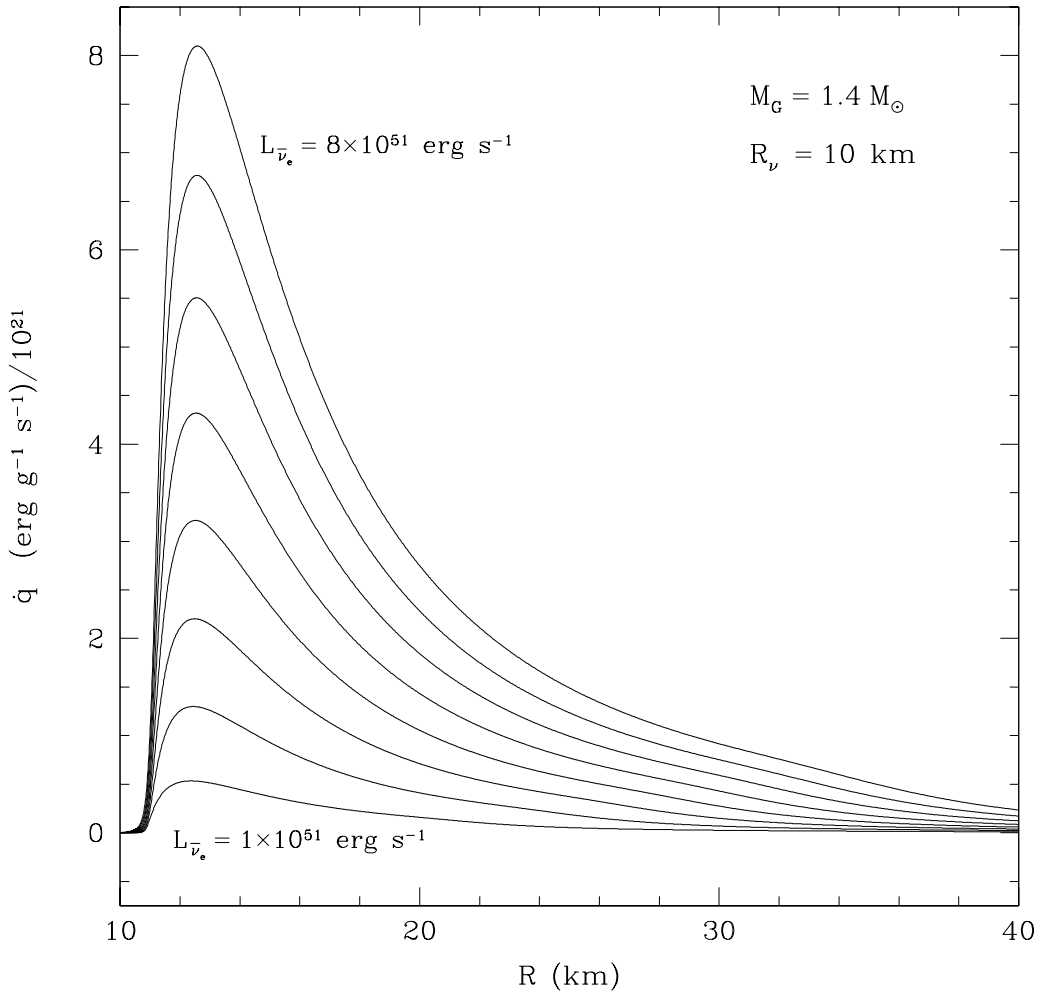


FIG. 4.— Energy deposition rate (\dot{q}) in units of $10^{21} \text{ erg g}^{-1} \text{ s}^{-1}$ as a function of radius (in km) for the wind models in Figs. 1–3. \dot{q} profiles for $\bar{\nu}_e$ neutrino luminosities from $8 \times 10^{51} \text{ erg s}^{-1}$ to $1 \times 10^{51} \text{ erg s}^{-1}$ are depicted. The total heating rates (Q ; eq. 14) for each of these models are given in Table 1.

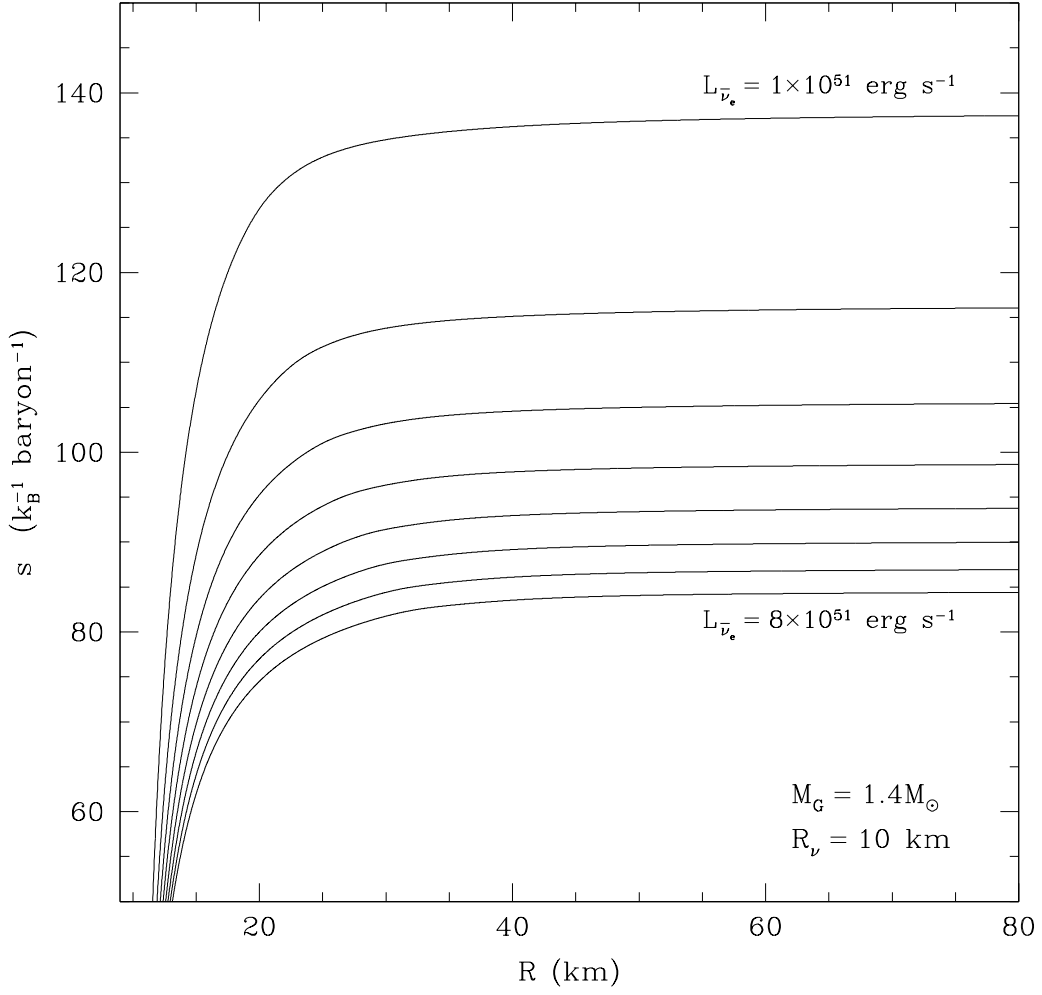


FIG. 5.—Entropy (s , per baryon per k_B) versus radius in km for the same protoneutron star wind models as in Figs. 1-4. Note that the entropy asymptotes quickly; comparing this figure to Fig. 3, we can see that in most cases s increases less than 10 units for $T < 0.5$ MeV.

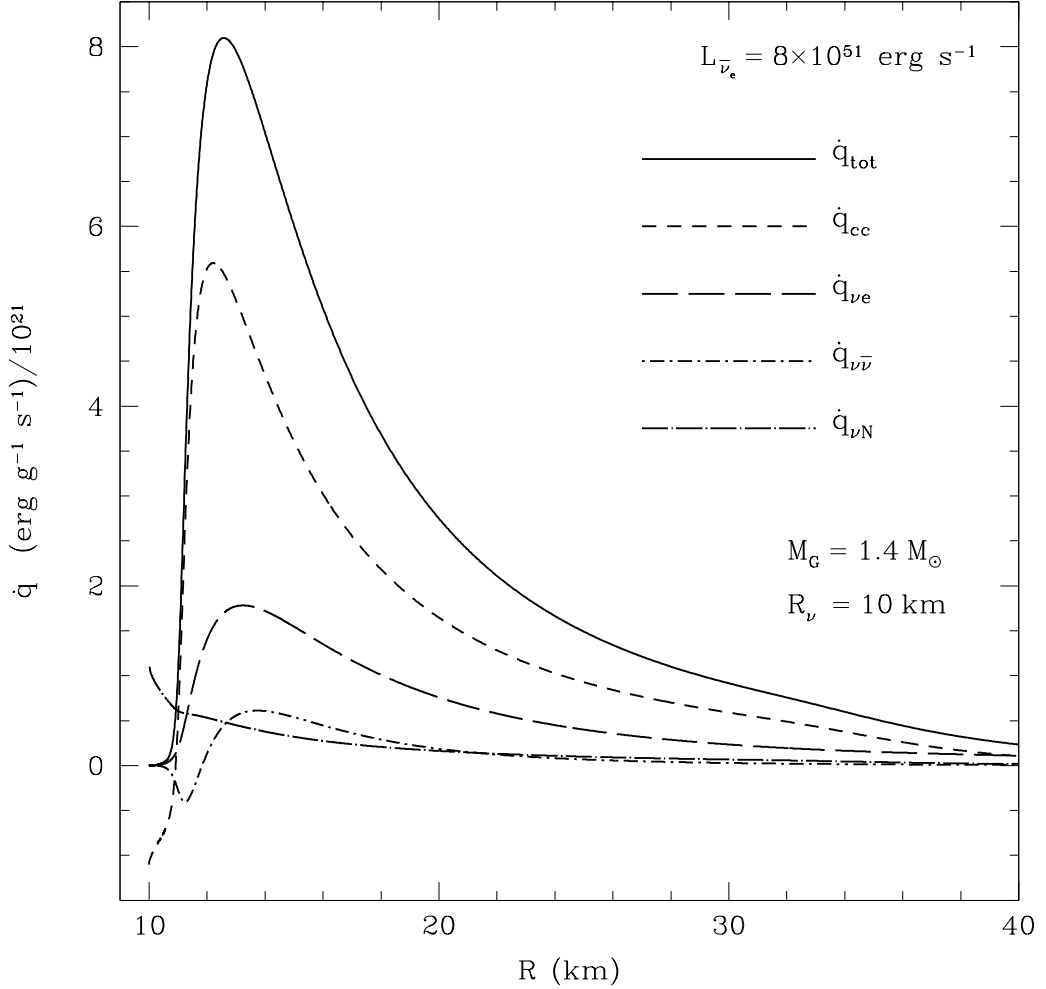


FIG. 6.— Contributions of specific neutrino processes to the energy deposition rate for $L_{\bar{\nu}_e} = 8 \times 10^{51} \text{ erg s}^{-1}$, $R_\nu = 10 \text{ km}$, and $M = 1.4 M_\odot$. The solid line shows the total heating rate due to all processes, the short-dashed line is the net contribution from the charged-current reactions (\dot{q}_{cc}) (eqs. 20 and 21), the long dashed line is neutrino-electron/positron scattering ($\dot{q}_{\nu e}$; eq. 27), the short dot-dashed line is the net energy deposition rate due to $\nu_i \bar{\nu}_i \leftrightarrow e^+ e^-$ ($\dot{q}_{\nu \bar{\nu}}$; eqs. 29 and 31), and the long dot-dashed line is for neutrino-nucleon scattering ($\dot{q}_{\nu N}$; eq. 28). Note the fairly rapid decrease in \dot{q}_{cc} at $r \sim 35 \text{ km}$ is due to the recombination of free neutrons and protons into α particles. As the neutrino luminosity decreases in these models, this transition moves inward in radius so that, for the lowest luminosities, the charged current processes end abruptly at $\sim 25 \text{ km}$. For models with larger M/R_ν $\dot{q}_{\nu e}$ and $\dot{q}_{\nu \bar{\nu}}$ become more important relative to \dot{q}_{cc} . However, even for $M = 2.0 M_\odot$ and $R_\nu = 10 \text{ km}$, \dot{q}_{cc} dominates at the peak in \dot{q}_{tot} .

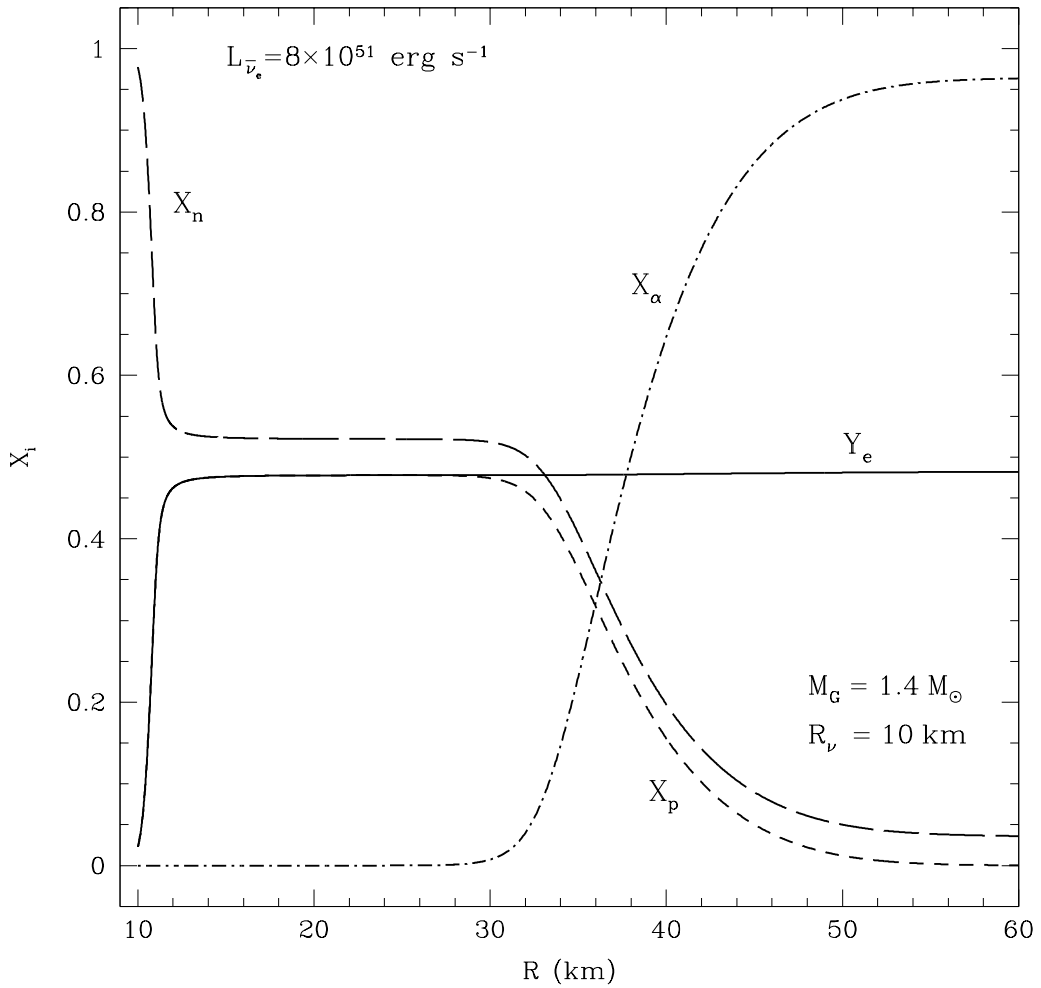


FIG. 7.— The electron fraction (Y_e , solid line), proton fraction (X_p , short dashed line), neutron fraction (X_n , long dashed line), and alpha fraction (X_α , dot-dashed line) for the highest luminosity wind model ($L_{\bar{\nu}_e} = 8 \times 10^{51} \text{ erg s}^{-1}$) in Figs. 1-5, corresponding to the heating profile in Fig. 6. Note the transition at $r \sim 35$ km where α particles form and effectively shut off the charged-current heating rate. The asymptotic Y_e is set very close to the neutron star ($r \sim 15$ km) and only undergoes small subsequent change as a result of the α -effect (Fuller and Meyer 1995; McLaughlin, Fuller, and Wilson 1996)). In this case, Y_e changes by $\sim 1\%$ beyond $r = 20$ km. The asymptotic electron fraction, Y_e^a , is well-approximated by eq. (16) in the text.

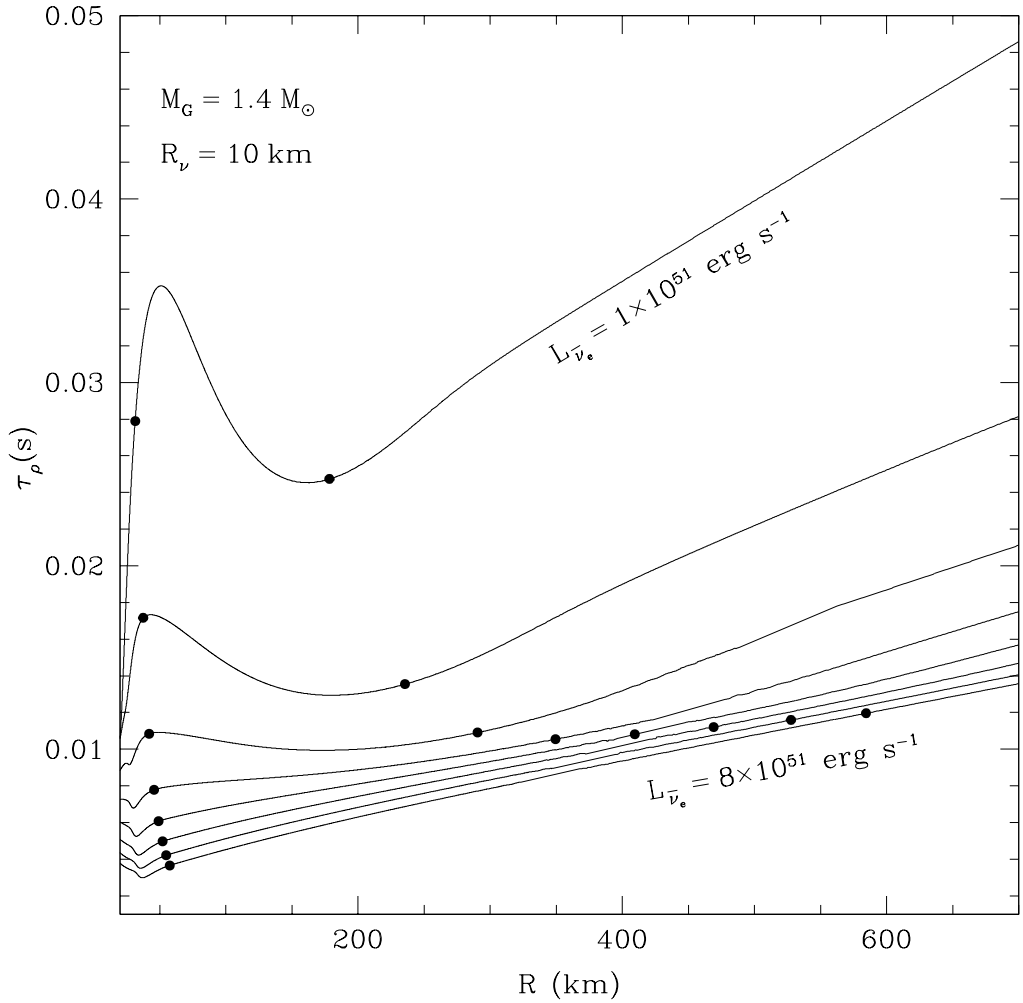


FIG. 8.— Dynamical timescale (τ_ρ) defined in eq. (32) versus radius for the eight models shown in Figs. 1-5. On each line, the first point marks the radius at which $T(r) = 0.5$ MeV. The second point marks where $T(r) = 0.1$ MeV. Note that for high luminosities, τ_ρ increases by more than a factor of three over the range of radii and temperatures relevant for r -process nucleosynthesis. For the lowest luminosities $d\tau_\rho/dr$ changes sign and τ_ρ actually decreases by $\sim 30\%$ between the two points on the $L_{\bar{\nu}_e} = 1 \times 10^{51}$ erg s $^{-1}$ curve.

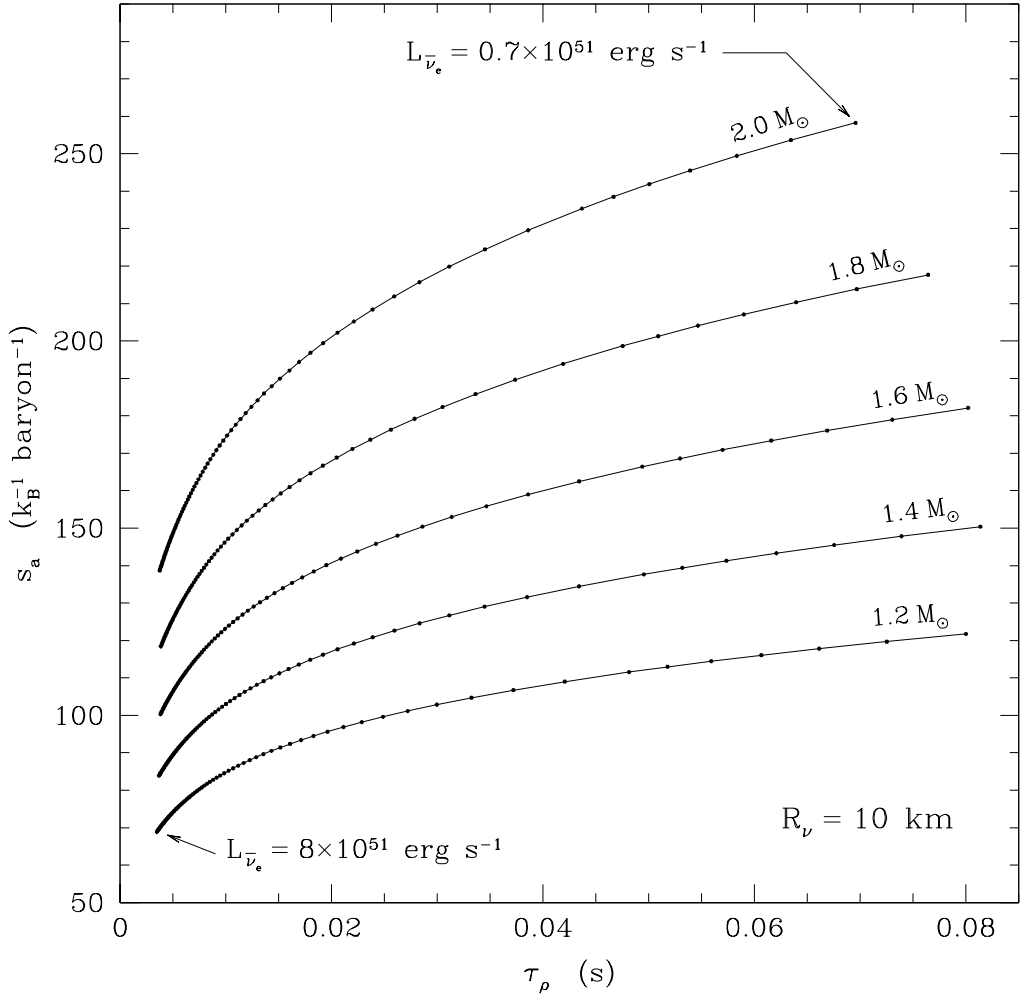


FIG. 9.—Tracks for constant protoneutron star mass in the plane of asymptotic entropy (s_a , per k_B per baryon) and dynamical timescale (τ_ρ , eq. 32) in seconds. R_ν is held constant at 10 kilometers. Each track covers a range in luminosity from $L_{\bar{\nu}_e} = 8.0 \times 10^{51}$ erg s^{-1} to $L_{\bar{\nu}_e} = 0.7 \times 10^{51}$ erg s^{-1} . Small dots are the points for which a model with a given luminosity was calculated. All masses are gravitational masses. In these models, we take $\langle \varepsilon_{\nu_e} \rangle = 11$ MeV, $\langle \varepsilon_{\bar{\nu}_e} \rangle = 14$ MeV, and $\langle \varepsilon_{\nu_\mu} \rangle = 23$ MeV for $L_{\bar{\nu}_e} = 8.0 \times 10^{51}$ erg s^{-1} . For each subsequent luminosity, the average energies were decreased according to $\langle \varepsilon_\nu \rangle \propto L_\nu^{1/4}$. In Table 1, we summarize the global properties at several luminosities along the $1.4 M_\odot$ trajectory in this figure.

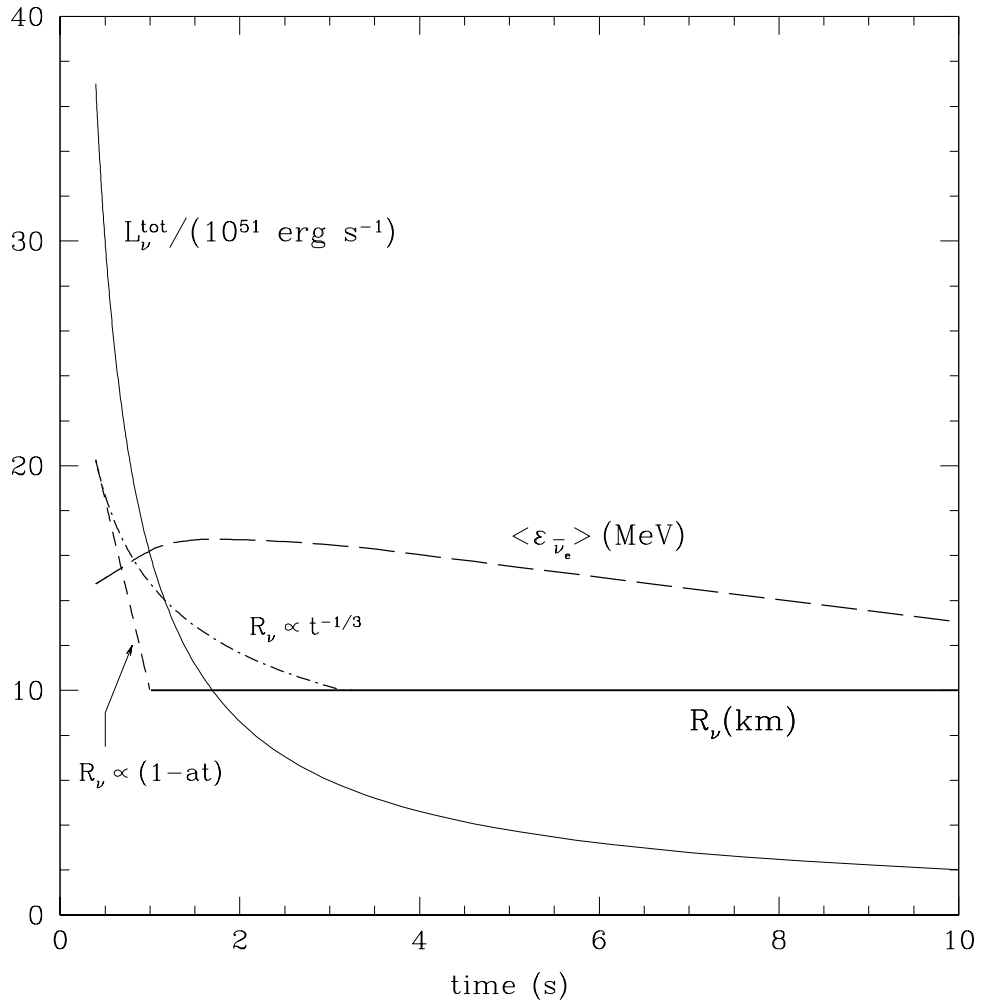


FIG. 10.—A schematic showing total neutrino luminosity in $10^{51} \text{ erg s}^{-1}$ (thin solid line), average $\bar{\nu}_e$ neutrino energy in MeV (long dashed line), and neutrinosphere radius (R_ν) in km. Two possible evolutions for $R_\nu(t)$ are shown. Linear contraction such that $R_\nu(t = 0.4 \text{ s}) = 20.3 \text{ km}$ and $R_\nu(t = 1 \text{ s}) = 10.0 \text{ km}$, which we label as ' $R_\nu(t) \propto 1 - at$ ', is shown as a short dashed line. Contraction with $R_\nu(t) \propto t^{-1/3}$ is shown as a dot-dashed line. The thick solid line denotes 10 km, the final R_ν for the protoneutron star. L_ν^{tot} is proportional to $t^{-0.9}$. We set $\langle \varepsilon_{\nu_\mu} \rangle / \langle \varepsilon_{\bar{\nu}_e} \rangle = 1.6$, $\langle \varepsilon_{\bar{\nu}_e} \rangle / \langle \varepsilon_{\nu_e} \rangle = 1.3$, $L_{\bar{\nu}_e} / L_{\nu_\mu} = 1.4$, and $L_{\bar{\nu}_e} / L_{\nu_e} = 1.3$.

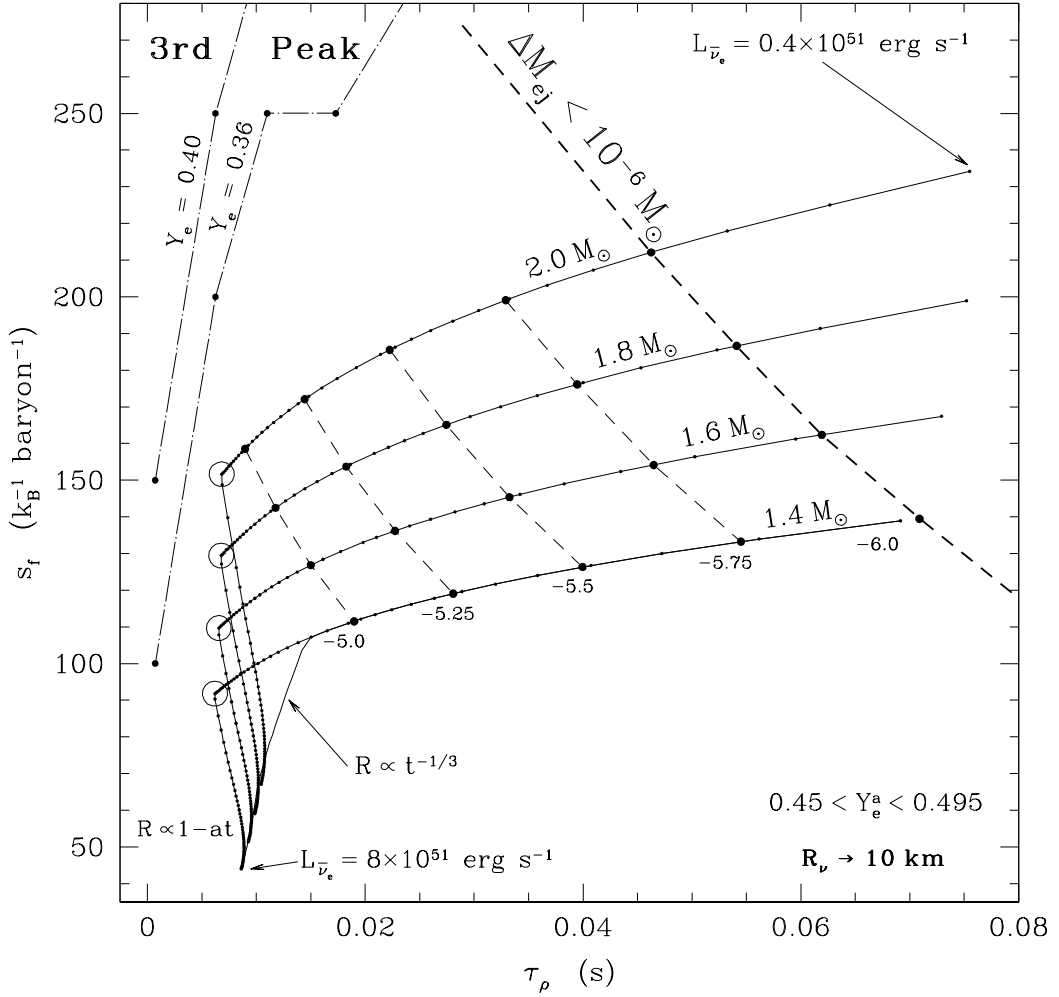


FIG. 11.—Evolutionary wind models in the plane of asymptotic entropy (s_a per k_B per baryon) and dynamical timescale (τ_ρ , eq. 32) in seconds. Tracks with $R_\nu(t) \propto (1-at)$ (see Fig. 10) for $M = 1.4, 1.6, 1.8$, and $2.0 M_\odot$ are shown as solid lines with small dots. The solid line without dots is the track with $R_\nu(t) \propto t^{-1/3}$ for $1.4 M_\odot$. All tracks start at small s_a and τ_ρ with $R_\nu \simeq 20.3$ km and $L_{\bar{\nu}_e}^{51} = 8.0$. The tracks end at high s_a and long τ_ρ with $L_{\bar{\nu}_e}^{51} = 0.4$. Taking $L_\nu \propto t^{-0.9}$, this range spans the first ~ 12 seconds of protoneutron star wind evolution. The large open circles mark $L_{\bar{\nu}_e}^{51} = 3.4$ for each mass trajectory. Dashed lines connecting all mass tracks with large dots are lines of constant $\log_{10}[\Delta M_{ej}]$ (see eq. 34, Fig. 13, and text for details). The dashed line connecting all mass tracks on the right, marked with -6.0 , delineates at what point in the evolution only $10^{-6} M_\odot$ of material is yet to be ejected. In all of the more than 350 models presented here the asymptotic electron fraction is always in the range $0.45 \leq Y_e^a \leq 0.495$. Generally, Y_e^a increases as the luminosity and average neutrino energies decrease. Finally, the dash-dotted lines in the upper left corner indicate, for constant values of Y_e^a , in what range of s_a and τ_ρ production of the third r -process abundance peak is possible in the calculations of Meyer & Brown (1997). See §6 for discussion and details.

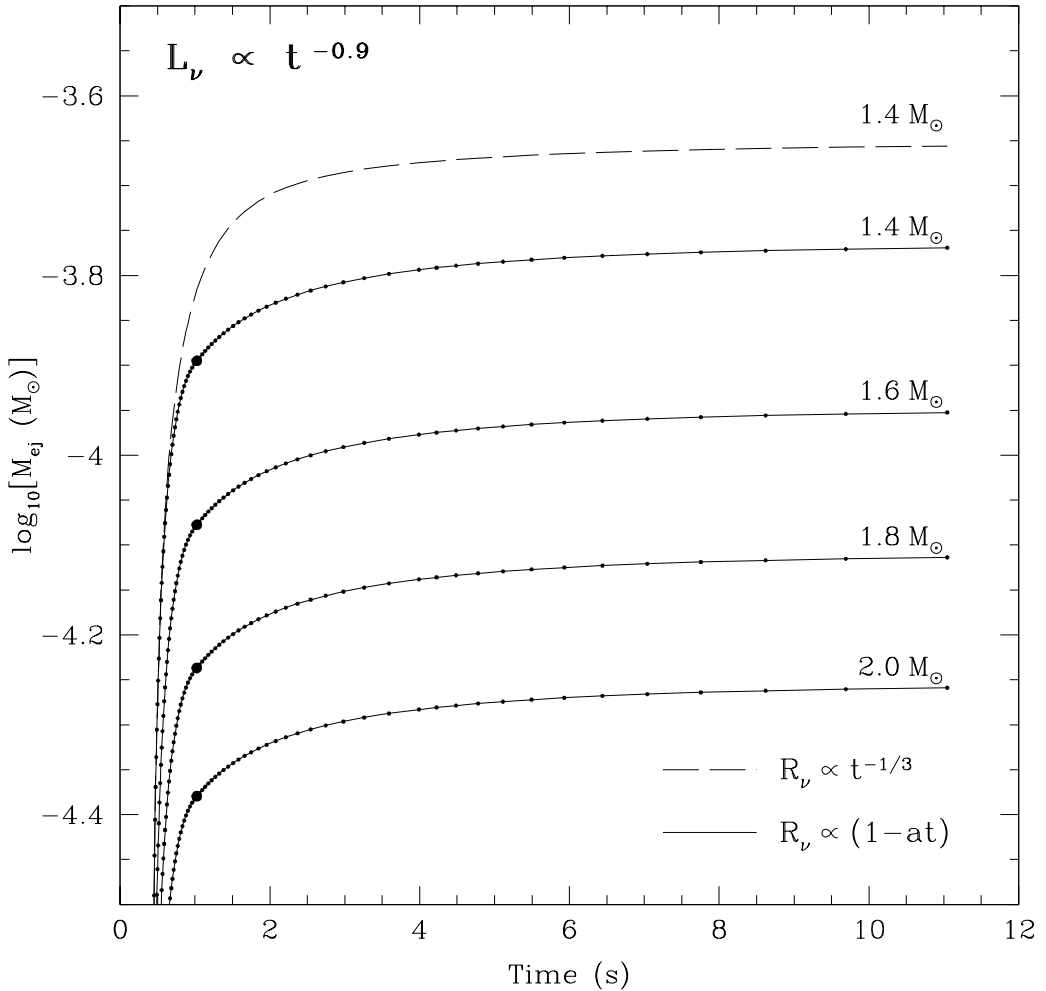


FIG. 12.—The log of the integrated total mass ejected M_{ej} (eq. 34) in units of M_{\odot} as a function of time in seconds, assuming $L_{\nu}(t)^{\text{tot}} \propto t^{-0.9}$ for the tracks of constant mass shown in Fig. 11. Evolutionary models with $R_{\nu}(t) \propto (1-at)$ (see Fig. 10) are shown as solid lines with small dots, which correspond to the dots in Fig. 11, indicating luminosity (time). M_{ej} for the track in Fig. 11 with $R_{\nu}(t) \propto t^{-1/3}$ and $M = 1.4 M_{\odot}$ is shown here as a long dashed line without dots. The large dot on each of the solid curves at $t \sim 1$ second shows the point at which the model has contracted to $R_{\nu} = 10$ km. This corresponds to the point on Fig. 11 where a given track of constant mass with $R_{\nu}(t) \propto (1-at)$ takes a sharp turn at $\tau_{\rho} \sim 0.006$ seconds.

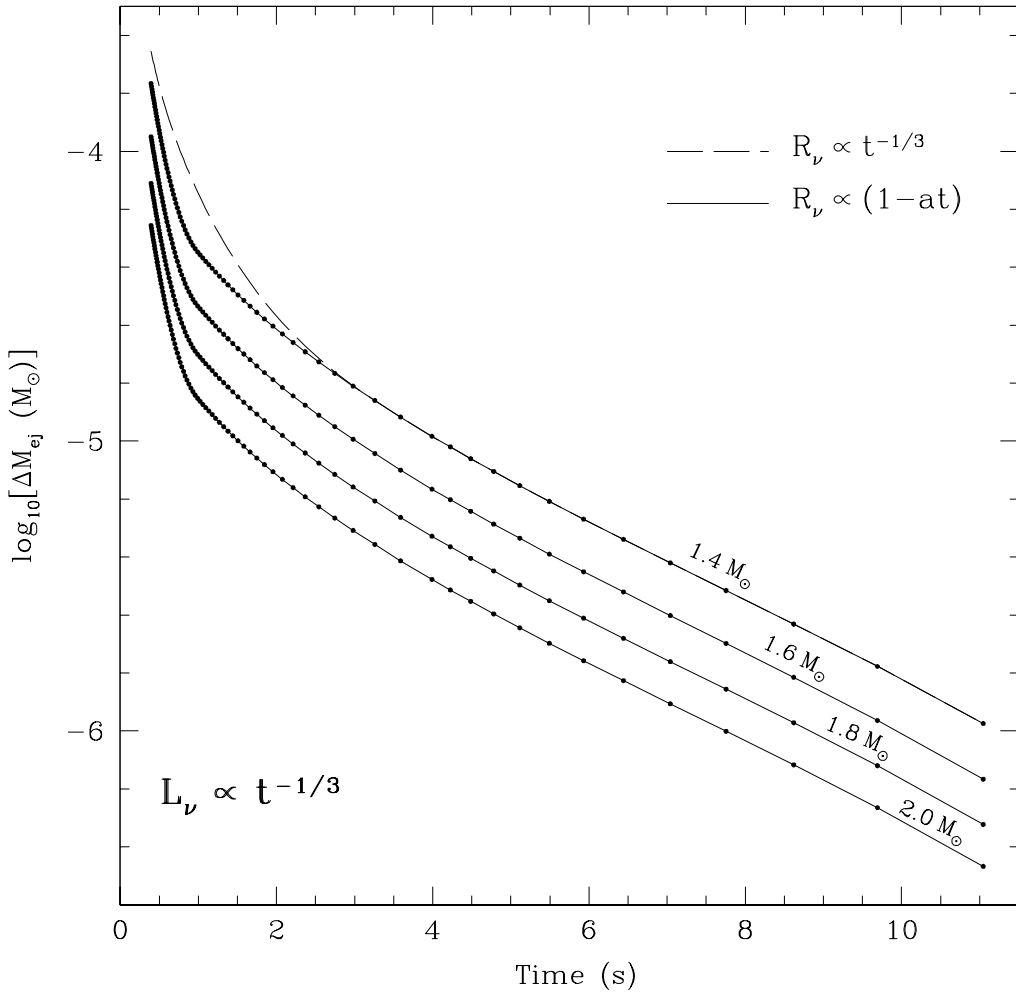


FIG. 13.— $\log_{10}[\Delta M_{ej} (= M_{ej}^{\text{tot}} - M_{ej}(t))]$, in units of M_\odot , versus time in seconds for the models in Fig. 12. The long dashed line is for the model with $R_\nu(t) \propto t^{-1/3}$. The four solid lines with dots correspond to those in Figs. 11 and 12 for the 1.4, 1.6, 1.8, and 2.0 M_\odot evolutionary models, which we label with ‘ $R_\nu(t) \propto 1-at$ ’. Lines of constant $\log_{10}[\Delta M_{ej}]$ are shown in Fig. 11 as dashed lines connecting big dots on the evolutionary models with $R_\nu(t) \propto (1-at)$.